



## RESEARCH ARTICLE

10.1029/2023JD040574

## Key Points:

- We present a new method for retrieving water and sulfate aerosol column densities from Open-Path Fourier-Transform Infrared measurements of near-source volcanic plumes
- Temperature-dependent  $\text{SO}_2/\text{SO}_4^{2-}$  ratios range from 100 in colder plumes to 250 in hotter plumes
- This method enables quantitative observation of primary aerosol formation in young plumes, a few seconds after emission

## Supporting Information:

Supporting Information may be found in the online version of this article.

## Correspondence to:

J.-F. Smekens,  
Jean-Francois.Smekens@nau.edu

## Citation:

Smekens, J.-F., Mather, T. A., Burton, M. R., Varnam, M., & Pfeffer, M. A. (2024). Rapid primary sulfate aerosol generation observed with OP-FTIR in the eruptive plume of the Fagradalsfjall basaltic eruption, Iceland, 2021. *Journal of Geophysical Research: Atmospheres*, 129, e2023JD040574. <https://doi.org/10.1029/2023JD040574>

Received 7 DEC 2023

Accepted 14 MAY 2024

## Author Contributions:

## Conceptualization: Jean-

François Smekens, Tamsin A. Mather, Mike R. Burton

Data curation: Jean-François Smekens, Tamsin A. Mather

Formal analysis: Jean-François Smekens, Tamsin A. Mather, Mike R. Burton

Funding acquisition: Tamsin A. Mather, Mike R. Burton

Investigation: Jean-François Smekens, Mike R. Burton, Matthew Varnam, Melissa A. Pfeffer

Methodology: Jean-François Smekens, Tamsin A. Mather, Mike R. Burton

## Rapid Primary Sulfate Aerosol Generation Observed With OP-FTIR in the Eruptive Plume of the Fagradalsfjall Basaltic Eruption, Iceland, 2021

Jean-François Smekens<sup>1,2</sup> , Tamsin A. Mather<sup>1</sup> , Mike R. Burton<sup>3,4</sup> , Matthew Varnam<sup>3,5</sup> , and Melissa A. Pfeffer<sup>6</sup>
<sup>1</sup>Department of Earth Sciences, University of Oxford, Oxford, UK, <sup>2</sup>Department of Astronomy and Planetary Science, Northern Arizona University, Flagstaff, AZ, USA, <sup>3</sup>Department of Earth and Environmental Sciences, University of Manchester, Manchester, UK, <sup>4</sup>National Institute of Geophysics and Volcanology INGV, Catania, Italy, <sup>5</sup>Lunar and Planetary Laboratory, University of Arizona, Tucson, AZ, USA, <sup>6</sup>Icelandic Meteorological Office, Reykjavik, Iceland

**Abstract** Open-Path Fourier-Transform Infrared (OP-FTIR) absorption spectroscopy is a powerful method for remote characterization of volcanic plume composition from safe distances. Many studies have used it to examine the composition of volcanic gas emitted at the surface, which is influenced by initial volatile contents and magma ascent/storage processes, and help to reveal the dynamics controlling surface activity. However, to evaluate the health hazard threats associated with volcanic emissions and their potential impact on wider atmospheric conditions, near-source particle measurements are also key. Here we present a forward model and fitting algorithm which allows quantification of particle size and abundance. This was successfully applied to radiometrically uncalibrated OP-FTIR spectra collected with a highly dynamic radiation source during the Fagradalsfjall eruption, Iceland, on 11 August 2021. Quantification of plume temperatures ranging from 350 to 650 K was essential to characterize the emission-absorption behavior of  $\text{SO}_2$ , enabling retrievals of particulate matter in the thermal infrared spectral window ( $750\text{--}1250\text{ cm}^{-1}$ ) in each spectrum. For the first time, we observe the rapid formation of primary aerosols in young plumes (only a few seconds old) with OP-FTIR. Temperature-dependent  $\text{SO}_2/\text{SO}_4^{2-}$  molar ratios range from 100 to 250, consistent with a primary formation mechanism controlled by cooling and entrainment of atmospheric gases. This novel aerosol spectrum retrieval opens new frontiers in field-based measurements of sulfur partitioning and volcanic plume evolution, with the potential to improve volcano monitoring and quantification of air quality hazard assessments.

**Plain Language Summary** Open-Path Fourier-Transform Infrared (OP-FTIR) spectroscopy is often used during volcanic eruptions to identify and quantify the amounts of different gases released during eruptions from a safe distance. This is important because gas compositions contain information about where magma came from and how it rose to the surface and erupted, and help us understand the impact of eruptions on air quality and climate. This paper presents a new way of analyzing spectra which allows us to quantify the amount and composition of aerosols, small droplets of water and other chemicals such as sulfuric acid. These aerosols can have important impacts on air quality and local climate, or even global climate in the case of large eruptions. We used this new approach during an eruption in 2021 on Iceland, pointing the instrument directly at the erupting vent, and were able to observe the formation of aerosols very close to their emission point, where they undergo rapid cooling. This is the first time we have been able to directly measure this aerosol formation process during an eruption. Our work opens new opportunities to re-analyze older data to extract further insights and provides new opportunities to better understand the impacts of future eruptions.

## 1. Introduction

Quantifying the composition and emission rate of gases released from a volcanic system is important because gas compositions are influenced by initial volatile contents and magma ascent/storage processes, thus revealing important information about the dynamics which control volcanic activity. For example, changes in the composition of volcanic emissions can precede shifts in eruptive behavior (Aiuppa et al., 2009, 2010; Moretti et al., 2018) and can be used to investigate subsurface magmatic processes (Burton et al., 2007). Volatile emissions are also critical inputs into the global cycles of carbon, sulfur, and water. Quantification of global volcanic gas fluxes is therefore among the key objectives for volcanology. Given that such measurements are usually underpinned by quantification of  $\text{SO}_2$  emissions, all processes which affect sulfur speciation within a

© 2024. The Author(s).

This is an open access article under the terms of the Creative Commons Attribution License, which permits use, distribution and reproduction in any medium, provided the original work is properly cited.

**Project administration:** Tamsin A. Mather, Mike R. Burton  
**Resources:** Jean-François Smekens, Matthew Varnam, Melissa A. Pfeffer  
**Software:** Jean-François Smekens  
**Supervision:** Tamsin A. Mather, Mike R. Burton  
**Visualization:** Jean-François Smekens  
**Writing – original draft:** Jean-François Smekens, Tamsin A. Mather, Mike R. Burton  
**Writing – review & editing:** Jean-François Smekens, Tamsin A. Mather, Mike R. Burton, Matthew Varnam, Melissa A. Pfeffer

plume are important to understand. One such key process is the oxidation of SO<sub>2</sub> to sulfuric acid and subsequent sulfate aerosol formation. New insights into the degree of SO<sub>2</sub> conversion at the point of emission and after further evolution are fundamental. Quantification of particulate matter (PM) concentration in plumes is also important for the accurate assessment of respiratory hazards associated with volcanic emissions (Allen et al., 2000; Ilyinskaya et al., 2017; Longo et al., 2010; Whitty et al., 2020). Moreover, the ratio between sulfur dioxide (SO<sub>2</sub>) and sulfate aerosols (SA) is a crucial input parameter for atmospheric dispersal models used to forecast plume transport (Beirle et al., 2014; Businger et al., 2015; Ilyinskaya et al., 2017; Schmidt et al., 2015).

### 1.1. Measuring Plume Composition Using OP-FTIR

One method used to measure plume composition remotely is Fourier-Transform Infrared (FTIR) spectroscopy. Most atmospheric gases have distinctive rotational and vibrational features in the near-infrared to the far-infrared spectral range, and the method has been used increasingly by the volcanic gas community over the past 30 years (Allard et al., 2005, 2016; Burton et al., 2007, 2023; Francis et al., 1998; Horrocks et al., 1999, 2001; La Spina et al., 2010; Mori et al., 1995; Mori & Notsu, 1997; Notsu et al., 1993; Oppenheimer et al., 1998). Using an Open-Path FTIR (OP-FTIR) spectrometer, the intensity of radiation can be accurately measured over a wide range of wavelengths, and if the source of infrared radiation has a higher temperature than infrared-absorbing gases between the source and the spectrometer then distinct absorptions can be quantified. The location of absorption lines allows identification of specific gas species, and the strength of the absorption allows for quantification. Quantification is typically in units of molecules.cm<sup>-2</sup>, which is equivalent to an assumed concentration in molecules.cm<sup>-3</sup> over an arbitrary pathlength of 1 cm, as the exact distribution of molecules along the line of sight cannot be readily ascertained.

Quantification of gas amounts is obtained by fitting a modeled spectrum to the measured spectrum (Burton et al., 2000, 2007). The source of IR radiation can be provided by hot eruptive material (lava flow, lava dome, lava fountains, etc.), in a geometry which we will refer to as direct line-of-sight (e.g., Burton et al., 2000, 2007; La Spina et al., 2015; Oppenheimer et al., 2006; Pfeffer et al., 2018). Alternatively, the IR signal can be generated by an artificial light source. This geometry is commonly used for grounded plumes or where it is possible to align the source and detector across the fuming crater (e.g., Horrocks et al., 1999; La Spina et al., 2010; Mori et al., 1995). Finally, the method colloquially known as solar/lunar occultation uses a celestial object (i.e., the Sun or Moon) as the source of radiation, and is often especially useful to probe more distal plumes (e.g., Burton et al., 2001; Butz et al., 2017; Duffell et al., 2001; Francis et al., 1998).

OP-FTIR measurements are routinely used for monitoring gas composition during fissure-fed effusive eruptions (Burton et al., 2000; La Spina et al., 2015; McGee & Gerlach, 1998; Oppenheimer et al., 2006), and the Icelandic Meteorological Office (IMO) used this tool during the fissure eruptions of Holuhraun in 2014 (Pfeffer et al., 2018) and Fagradalsfjall in 2021 (Halldórsson et al., 2022). The method, however, is typically limited to the quantification of gas species, and only a few recent studies have attempted to quantify aerosol abundance in volcanic plumes using FTIR spectra. Sellitto et al. (2019) showed that the simultaneous retrieval of SO<sub>2</sub> and sulfate aerosols is possible from active absorption measurements (i.e., with an artificial IR lamp), applying the principles of differential absorption spectroscopy to extract the transmission of the volcanic plume against a clear (free of volcanic gases) spectrum acquired in an identical geometry. In that configuration, the assumption can be made that the intensity of the IR source remains constant between measurements, and spectra can be ratioed to isolate the plume transmission from individual measurements. More recently, Smekens et al. (2023) quantified ash and sulfate aerosol abundances in the plume of Stromboli in Italy, using radiometrically calibrated spectra taken in an emission geometry (i.e., where the measured radiation is that of the plume itself, against a relatively colder clear sky background).

Here we show that quantitative retrievals of particulate species in a traditional (i.e., usually the most readily employed during volcanic monitoring) direct line-of-sight (LOS) geometry are possible - assuming a certain linearity in the instrument response over the thermal infrared retrieval window - and present the first measurements of sulfate aerosol using this method in the passive plume emitted during the 2021 eruption of Fagradalsfjall in Iceland, allowing us to investigate sulfur speciation within the plume.

## 1.2. The 2021 Fagradalsfjall Eruption

On 19 March 2021, an effusive eruption started on the Reykjanes peninsula in southwest Iceland. The eruption, the first on the peninsula in almost 800 years (Sæmundsson et al., 2020), followed a 14-month long period of seismic unrest (Greenfield et al., 2022), culminating in the intrusion of a dyke within the Fagradalsfjall region (Sigmundsson et al., 2022). The eruption was characterized by four phases of activity (Barsotti et al., 2023). During the first few weeks (Phase I: 19 March–5 April 2021), activity was confined to a single vent and characterized by continuous effusion of a lava flow field. In Phase II (5–27 April), additional vents opened along the orientation of the original dyke, and lava was erupted from multiple vents simultaneously. Phase III (27 April–28 June) saw the concentration of activity back to a single vent, and the start of intense pulsating lava fountains. The intensity of the fountains then decreased in Phase IV (28 June–18 September), during which lava effusion occurred from the main vent in a cyclical manner with pauses in activity lasting for several hours. All phases of activity were associated with the emission of a plume of gas and particulate matter (PM), presenting a series of hazards to nearby communities (Barsotti et al., 2023; Carlsen et al., 2021; Gudmundsson, 2011; Horwell, 2007; Ilyinskaya et al., 2017; Tang et al., 2020). In this study, we look at the composition of the volcanic plume during the phase of cyclic activity (Phase IV) using field observations acquired on 11 August 2021.

## 2. Methods

### 2.1. Direct LOS OP-FTIR Measurements

The data set presented in this study (Smekens et al., 2024) was acquired over a period of approximately 30 min in the early hours of 11 August 2021 (local time). Spectra were recorded continuously with the OP-FTIR instrument pointing directly at the crater of the eruptive vent during a phase of high activity, with the objective of characterizing plume composition at the point of emission. During this part of the eruption, the cycle duration at the vent was approximately 24 hr, with periods of lava effusion lasting for 8–10 hr. During the effusive episodes, vigorous bubbling was observed within the crater, sometimes producing small fountains a few tens of meters high. This activity sustained a strong plume of gases and aerosols which rose to altitudes of 1–2 km before drifting with the prevailing wind direction of the day. The data presented in this study was acquired with an OP-FTIR spectrometer in direct line-of-sight to the vent.

The spectra were acquired with a Midac M4401-SP spectrometer. Light is directed through a Michelson interferometer equipped with a ZnSe beam splitter and toward a single-element Stirling pump cooled Mercury-Cadmium-Telluride (MCT) detector. The internal telescope uses all-reflective optics (gold-coated concave mirrors) and has a field-of-view (FOV) of  $\sim 20$  mrad. The spectrometer is powered with a 12V car battery and operated with a laptop and the Essential FTIR software. Spectra were acquired over the spectral range 600–4,500  $\text{cm}^{-1}$ , averaging 4 scans to reduce noise, and with a spectral sampling of  $\sim 0.25$   $\text{cm}^{-1}$ , which resulted in a sampling interval of approximately 3.5 s between consecutive measurements.

The measurement site was located on an elevated ridge, approximately 1.22 km to the southeast of the active vent, giving a direct view into the opening of the crater (Figure 1b). The exact location of the FOV is difficult to determine, as the alignment was done manually, looking for the position giving the strongest signal to maximize signal-to-noise ratio (SNR). At a distance of 1.22 km, the FOV would cover a circle with a diameter of approximately 25 m. The width of the lava pond within the crater at the time was larger than 25 m, however, the FOV may not always have been filled with incandescent material. As the mild fountaining activity waxed and waned, the fraction of the FOV filled with incandescent material varied quickly, resulting in a highly dynamic source of radiation, and rapid fluctuations in the intensity of the measured signal from one spectrum to the next.

The plume itself was also very dynamic. At times, we suspect older parts of the plumes may have drifted back into our line-of-sight, although direct observation of this phenomenon was difficult. As well, the line-of-sight ran over the active lava flow, which was still visibly degassing. This means that in addition to the very young plume emitted at the vent, we also captured varying amounts of more mature plumes and gases from the degassing of the lava flow, both of which are likely to exhibit a composition different from the main plume, and constitute another source of variability when interpreting our plume composition results.

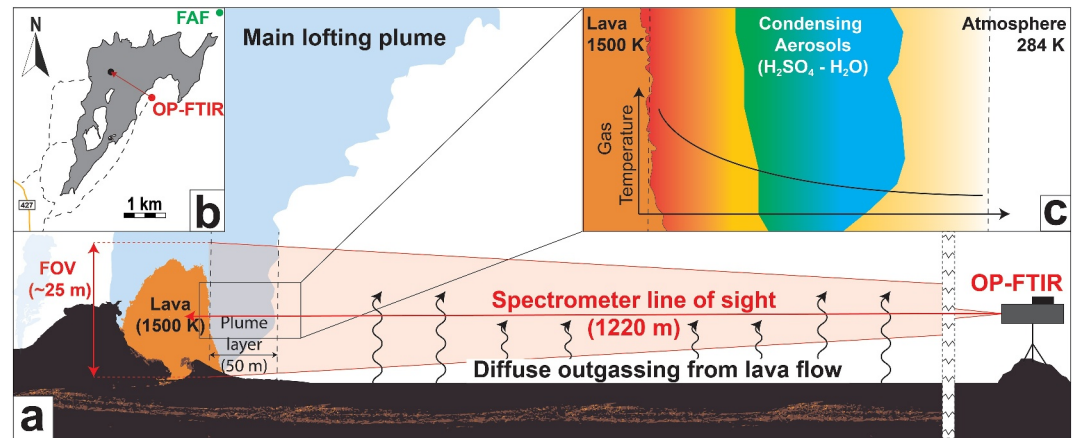


**Figure 1.** Conceptual representation of the viewing geometry for the Open-Path Fourier-Transform Infrared (OP-FTIR) measurements on 11 August 2021. During active phases, the crater was filled with a lava pond with a sustained lava fountain. Sustained activity produced a main plume and the effusion of a lava flow, which also exhibited minor diffuse outgassing. (a) Side-view of the measurement along the line-of-sight. (b) Map of the lava flow field extent as of 30 September 2021 (modified from Barsotti et al., 2023) showing the location of the OP-FTIR instrument (red circle) relative to the active vent. Access footpaths and service roads are shown as dashed lines. Also shown is the location of the FAF seismic station (green circle). (c) Zoom in on the plume zone at the edge of the lava fountain. Very hot gas is present close to the lava surface, and the temperature rapidly decreases with distance. Aerosols start condensing as the plume cools down. Spectral models presented in this study assume a single temperature for the hot gas, which is an oversimplification of the thermal complexity depicted here.

## 2.2. Retrieval Algorithm

The data analysis was performed using a retrieval algorithm adapted from the one originally developed by Smekens et al. (2023) for emission measurements, with the explicit aim of quantifying volcanic aerosols in transmission geometries. The code presented here (Smekens, 2024) is an extension of the original software and is also available as an open-source Python3 code at <http://www.github.com/jfsmekens/plumeIR>. The iterative forward model and non-linear least squares fitting routine are retained and applied to a simplified transmission geometry identical to that used in the commonly used FTIR\_FIT software (Burton et al., 2000, 2007). A list of the fitting windows used in this study is presented in Table 1. A series of additional parameters have been added for the retrieval of sulfate aerosols over the Thermal Infrared (TIR) region of the spectrum ( $750\text{--}1250\text{ cm}^{-1}$ ).

The geometry is defined with a two-layer atmosphere (one for hot volcanic gas and the other for ambient temperature atmospheric gases). Each layer is assumed to be homogeneous and is defined by a unique temperature, pressure, and thickness. The forward model replicates the signal produced by the source of IR radiation (i.e., the lava surface from a flow or fountain) passing through both layers following:

**Table 1**  
Fitting Windows Used in Spectral Fits for the FTIR Data

Fitting window <sup>a</sup> ( $\text{cm}^{-1}$ )	Atmospheric layer (1220 m)	Volcanic layer (50 m)
750–1250	$\text{H}_2\text{O}$ , $\text{CO}_2$ , $\text{CH}_4$ , $\text{N}_2\text{O}$ , $\text{O}_3$	$\text{SO}_2$ (g), $\text{SO}_4^{2-}$ (aq), $\text{H}_2\text{O}$ (l)
2020–2150	$\text{N}_2\text{O}$ , $\text{H}_2\text{O}$ , $\text{CO}_2$	$\text{CO}$
2450–2550	$\text{N}_2\text{O}$ , $\text{H}_2\text{O}$ , $\text{CH}_4$	$\text{SO}_2$
2690–2830	$\text{N}_2\text{O}$ , $\text{H}_2\text{O}$ , $\text{CH}_4$	$\text{HCl}$
4020–4060	$\text{H}_2\text{O}$	$\text{HF}$

*Note.* Target species are denoted in bold. <sup>a</sup>Note that  $\text{H}_2\text{O}$  and  $\text{CO}_2$  are retrieved as atmospheric gases.  $\text{SO}_2$  is retrieved using the  $\nu_1 + \nu_3$  feature in a dedicated retrieval window at  $2500\text{ cm}^{-1}$  and also along with the particulate species in the TIR window using the  $\nu_1$  feature.

$$I(\tilde{\nu}) = B_t F(\tilde{\nu}) e^{-\tau} \quad (1)$$

where  $I$  is the measured intensity of the signal at the sensor (single beam) as a function of wavenumber  $\tilde{\nu}$ ,  $B_t$  is the blackbody radiance emitted by the radiation source (in this case, lava) at temperature  $t$ ,  $\tau$  is the cumulative optical depth of both layers, and  $F(\tilde{\nu})$  is the instrument response function (IRF) with respect to wavenumber over the fitting window. In order to accurately retrieve the slant column densities (SCD) for species with broad spectral features such as particulate species, a full radiometric calibration would ideally be performed to determine  $F(\tilde{\nu})$  for the specific instrument using a set of blackbodies at temperatures representative of the expected target range. While such calibration is possible in laboratory settings, it would be impractical to implement in the field for direct LOS measurements, where the source temperatures are expected to be very high (up to 1500 K for the typical eruptive temperatures of a basalt). Instead, if we assume the IRF to be linear over the fitting window used for particulates (750–1250  $\text{cm}^{-1}$  or approximately 8–12  $\mu\text{m}$ ), we can represent the product of the IRF and the Planck function as a relatively smooth and uniform “background” signal with a low degree polynomial (i.e.,  $p = 3$ ). The detectivity of a MCT detector across the thermal infrared window, though not linear, can be approximated by a second-order polynomial function (Sizov et al., 2008). Further spectral variations can then be attributed to the extinction by particulate matter (PM) species.

For gas species, we generate reference optical depth spectra using the Reference Forward Model (RFM version 5) (Dudhia, 2017). The model uses line data and reference cross-sections extracted from the high-resolution transmission molecular absorption database (HITRAN, Rothman et al., 2009; Gordon et al., 2022). A single reference optical depth spectrum is calculated for each species ( $\tau_{i,ref}$ ), using the corresponding layer thickness and a reference SCD, which is translated into a volume mixing ratio (VMR,  $\rho_{i,ref}$ ) based on the temperature and pressure assigned to each layer. For particulate species, the reference optical depth spectrum is generated following the principles of Mie scattering using the PyMieScatt software (Sumlin et al., 2018), assuming a reference mass column density, which is translated into a number concentration based on the density of the aerosol and the effective diameter of the particles  $d_{eff}$ . The optical depth of the homogeneous layer can then be calculated by scaling the reference spectra according to the ratio between the actual VMR in the layer ( $\rho_i$ ) and the reference VMR and summing the contributions of all species:

$$\tau = \sum_i \frac{\rho_i}{\rho_{i,ref}} \tau_{i,ref} \quad (2)$$

Each species is classified as either atmospheric or volcanic, each with its own temperature. The atmospheric layer thickness is defined as the distance between the source of radiation and the instrument and is assumed to be  $\approx 50$  m for the plume layer. For particulate species, we only consider single scattering effects, and therefore assume a linear relationship between particulate concentration and optical depth as expressed in Equation 2. While in the case of gaseous species, the layer thickness is relatively unimportant in determining the SCD along a prescribed path, the same cannot be said for particulate matter (PM). Assigning a realistic thickness to the volcanic layer is crucial, as the shape of the absorption spectra is defined by Mie scattering effects, which in turn depend on the number density ( $N$ ), and not just on the integrated column densities.

The dependence of the reference spectrum on non-linear parameters is also modeled using a type of look-up tables. For example, the existence of a continuum absorption affecting water vapor spectra makes the use of Equation 2 inaccurate for the  $\text{H}_2\text{O}$  species. Instead, we calculate a series of reference spectra for a range of scaling factors (0–2) applied to a reference  $\text{H}_2\text{O}$  SCD, and use a polynomial relationship to represent the dependency of the optical depth to the adjusted VMR at each wavenumber  $\tilde{\nu}$  over a given fitting window:

$$\tau_{\alpha,\tilde{\nu}} = \sum_{j=0}^p c_{j,\tilde{\nu}} \alpha^j \quad (3)$$

where  $\alpha$  is the  $\text{H}_2\text{O}$  scaling factor,  $p$  is the degree of the polynomial, and  $c_j$  is the coefficient in the polynomial expression for the term of degree  $j$ . In a similar manner, we introduce a dependency of the optical depth reference spectrum for PM on particle size. We quantify the relationship between effective particle diameter and the reference optical depth at each wavenumber as:



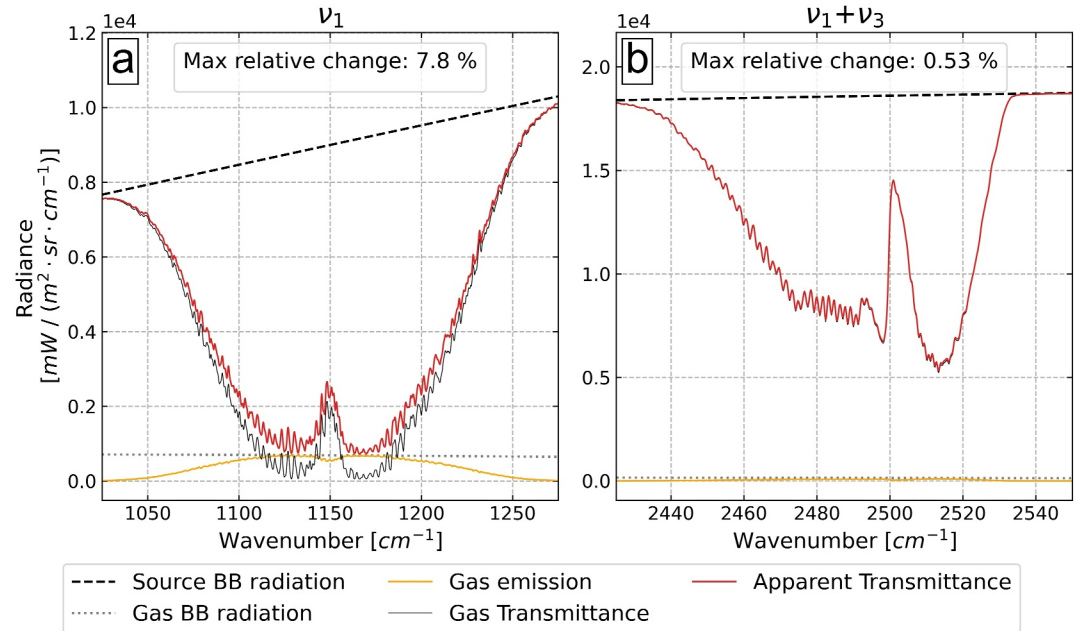


**Figure 2.** Simulated transmission of a pure  $\text{SO}_2$  layer ( $1 \times 10^{20} \text{ molec}\cdot\text{cm}^{-2}$ ) at 500 K in front of a blackbody source at 1500 K. Results are shown over the  $\nu_1$  feature (a) and the  $\nu_1 + \nu_3$  feature (b). The radiance of the source is assumed to be a blackbody (dashed black lines). Transmittance of the  $\text{SO}_2$  layer is shown in black, and the emission of the gas is shown in orange. The apparent transmittance (i.e., the signal measured by an observer) is shown in red. Also shown is the blackbody radiation at gas temperature (dotted gray line). All spectra have been convolved with the spectrometer instrument line shape. The relative change in apparent transmittance is much higher in the TIR spectral window.

$$\tau_{i,d_{eff},\tilde{\nu}} = \sum_{j=0}^n c_{j,\tilde{\nu}} d_{eff}^j \quad (4)$$

where  $d_{eff}$  is the mean effective diameter of the particles for species  $i$  (either ash or SA). This allows the model to accurately calculate optical depth spectra for any continuous value of  $d_{eff}$  within the bounds considered in the reference set (typically 0.1–10  $\mu\text{m}$ ). Finally, we use the same approach to represent the dependence of the absorption reference optical depth spectrum of a volcanic gas to the temperature of the layer  $t_{gas}$ :

$$\tau_{i,t_{gas},\tilde{\nu}} = \sum_{j=0}^n c_{j,\tilde{\nu}} t_{gas}^j \quad (5)$$

While in most gas retrievals, the radiative transfer can be solved with a purely transmissive geometry, the thermal complexity of the scene must be considered in its entirety at lower wavenumbers. Specifically, the emission of radiation by the volcanic gases must be accounted for. Figure 2 shows an example of the relative contribution of emitted radiation on the measured absorption of radiation for two of the spectral features associated with  $\text{SO}_2$  gas: the  $\nu_1$  feature at  $1150 \text{ cm}^{-1}$ , and the  $\nu_1 + \nu_3$  feature at  $1450 \text{ cm}^{-1}$ , both of which are used in this study. We modeled the transmittance of a simple volcanic layer with hot  $\text{SO}_2$  gas at 500 K, placed in front of blackbody source at 1300 K, with and without adding the radiation of the gas itself. While at higher wavenumbers in the  $\nu_1 + \nu_3$  band, the addition of the gas emission is negligible (<1% of the original signal), the same cannot be said for the  $\nu_1$  feature, where the resulting difference in measured signal would reach 8%. If the thermal contrast between the source and the gas is decreased (e.g., if the lava temperature is not uniform within the FOV), the relative contribution of the emission term can be even greater. For example, this may be the case when the source is a lava fountain or a bubbling pond, and pyroclasts only partially fill the field of view. Note that the relative shapes of the Planck blackbody functions for the gas and the source introduce a slope in the resulting corrected emission term. We found that accurately modeling the transmittance of  $\text{SO}_2$  in the  $\nu_1$  band requires the addition of

the emitted gas contribution. Therefore, the relatively simple forward model described in Equation 1 is modified as follows:

$$I(\tilde{\nu}) = \left( B_{rl} e^{-\tau_{volA}} + \frac{B_{l_{gasE}}}{B_{l_{source}}} (1 - e^{-\tau_{volE}}) \right) * e^{-\tau_{atm}} F(\tilde{\nu}) \quad (6)$$

where  $t_{gasE}$  and  $t_{source}$  are the temperatures of the hot gas and of the source, respectively,  $\tau_{atm}$  is the optical depth of the atmospheric layer,  $\tau_{volA}$  is the optical depth of the volcanic layer including all species (gas and PM), and  $\tau_{volE}$  is the optical depth of the volcanic gases only (without the PM species). The assumption is that the aerosol species are only present in the lower temperature parts of the plume where they are able to condense, and therefore their relative emission contribution can be ignored.

### 3. Results

#### 3.1. Combined Retrieval of SO<sub>2</sub> and Gas Temperature

Vigorous degassing often results in a very turbulent plume in the area just above the lava, creating an inhomogeneous plume and leading to very sharp increases and decreases in measured gas concentration. Such was the case during our measurements, and we observed rapid variations in degassing intensity, both in terms of gas concentration and gas temperature, over the course of the relatively short (30 min) data set presented here. For this reason, it is not appropriate to assume a single volcanic gas temperature over the course of the measurements. Instead, we use the  $\nu_1 + \nu_3$  absorption feature of SO<sub>2</sub> (2450–2550 cm<sup>−1</sup>) to retrieve SO<sub>2</sub> SCD and gas temperature simultaneously. The absence of strong interfering lines from H<sub>2</sub>O or CO<sub>2</sub> within that window allows for fitting of the target gas feature more directly. The shape of the  $\nu_1 + \nu_3$  feature depends strongly on the temperature of the gas, which allows us to parameterize gas temperature and retrieve it along with the SO<sub>2</sub> SCD. Accurate determination of this temperature is crucial to establishing reliable ratios, as the strength of absorption features for other species are also affected by gas temperature, but not always in a proportional manner.

Figure 3b shows the results of the combined retrieval. SO<sub>2</sub> SCDs range from  $1 \times 10^{19}$  to  $2 \times 10^{20}$  molec·cm<sup>−2</sup>, with very high variations from spectrum to spectrum, with gas temperatures ranging from 350 to 650 K. There is a general correlation between the retrieved SCD and gas temperature, with higher temperatures corresponding to higher SCDs. This can be interpreted in the context of a bubbling lava surface, with frequent bubble bursts releasing hot, concentrated gas. Assuming a single gas temperature (for example, the mean retrieved temperature of 450 K) can lead to significant errors of up to 30%, with overestimates when the gas is colder than assumed and underestimates when the gas is warmer (Figure 3c). Similar errors will affect the retrieval of other gases to varying degrees, considering the effect of temperature is different from one species to the next, or even from one absorption line to the next on a single gas species.

#### 3.2. Gas Composition

In addition to SO<sub>2</sub>, we retrieved time series of gas SCDs for the following gases: CO<sub>2</sub>, H<sub>2</sub>O, HCl and HF (spectral windows listed in Table 1). Errors introduced by inaccurate gas temperatures as outlined in Section 3.1 would significantly affect the derived gas ratios and overall composition. Therefore, following the method introduced by La Spina et al. (2015), we take the temperature retrieved with the SO<sub>2</sub>  $\nu_1 + \nu_3$  feature and impose it on a spectrum-by-spectrum basis for all other windows. As the atmospheric pathlength (1.22 km) is much larger than the assumed plume thickness (50 m), the majority of the H<sub>2</sub>O and CO<sub>2</sub> columns (>85% in all our measurements) are expected to be of atmospheric origin, and those two gases are retrieved as atmospheric gases, assuming the temperature and pressure recorded at the measurement site (284 K, 973 mb). Figure 4 presents scatter plots between retrieved column amounts for pairs of selected target gases. The ratio between two target species is derived using an Orthogonal Distance Regression (ODR), method, which allows for the treatment of errors in the so-called “independent” variable. ODR is well-suited to the regression of OP-FTIR data, where all gases have associated measurement errors. It produces ratios that are reciprocal regardless of which gas species is used on the x- or y-axis. SO<sub>2</sub> can be used as a tracer of volcanic origin, as all other gases show positive correlation with its abundance. Using the ratios in Figure 4, we derive the molar and mass composition of the gas for the measurement sequence taken as a whole, which we detail at the top of the figure. The measurements of volcanic gas ratios we obtained at the vent are in relatively good agreement with values measured using OP-FTIR earlier in the course of

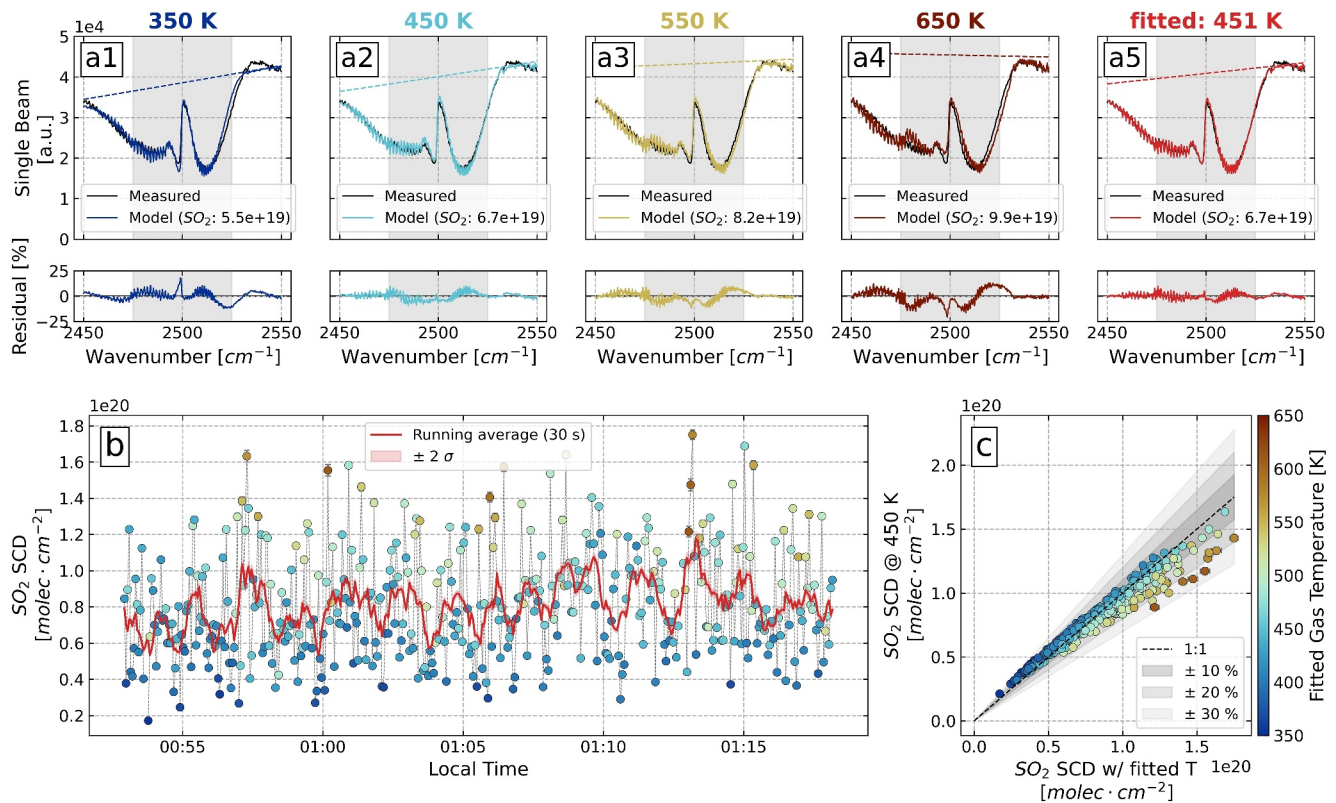


**Figure 3.** Results of the SO<sub>2</sub> retrieval and gas temperature determination. (a1-5) Spectral fits over the  $\nu_1 + \nu_3$  SO<sub>2</sub> feature for an example spectrum assuming four increasing gas temperatures, and the results of a fit where the gas temperature is fitted as a free parameter (a5). (b) Time series of retrieved SO<sub>2</sub> SCDs. Data points are colored according to the retrieved gas temperature. Note the general correlation between the two, with higher SCDs associated with higher temperatures. The red line is a 30 s running average to outline changes in outgassing on longer periods. (c) Scatter plot of SO<sub>2</sub> SCDs retrieved assuming a single temperature of 450 K against SO<sub>2</sub> SCDs retrieved with the gas temperature as a free parameter.

the eruption (Halldórsson et al., 2022; Scott et al., 2023). The ambient concentration of an atmospheric gas can be derived from the projected linear regression intercept, and subsequently corrected for when looking at the ratio for each individual data point. Using the CO<sub>2</sub>/SO<sub>2</sub> relationship, the ambient CO<sub>2</sub> concentration is estimated at 401 ppm. Using the H<sub>2</sub>O/SO<sub>2</sub> relationship, we can estimate the ambient relative humidity at 57%. These values are in reasonable agreement with the expected CO<sub>2</sub> content of the background atmosphere (~400 ppm) and the measured relative humidity at the measurement site (64%). Using the CO/SO<sub>2</sub> relationship, we can also estimate the background CO concentration at 119 ppb, which is within the range of expected concentrations in the lower troposphere (Borsdorff et al., 2018; George et al., 2015; Kumar et al., 2013; Reichle et al., 1982). The HCl/SO<sub>2</sub> scatter plot (Figure 4c) shows a positive intercept at  $5 \times 10^{17}$  molec · cm<sup>-2</sup>. Although it is possible that this offset is introduced by diffuse degassing of relatively sulfur-poor and chlorine-rich gases from the lava flow, we believe it is unlikely as the offset appears systematic and any interference from another gas source would likely not be so stable. Instead, we believe it is due to a minor systematic misfit, probably due to interference from water absorptions in the HCl fitting window. We highlight that this offset, unless corrected, would create a non-linear behavior in HCl/SO<sub>2</sub> ratios, with ratios increasing with decreasing concentrations.

### 3.3. Aerosol Composition

Aerosols are retrieved over a broad spectral window (750–1250 cm<sup>-1</sup>). A number of atmospheric gases are considered in the retrieval (H<sub>2</sub>O, CO<sub>2</sub>, CH<sub>4</sub>, N<sub>2</sub>O, O<sub>3</sub>), as well as SO<sub>2</sub> as a volcanic gas. H<sub>2</sub>O and CO<sub>2</sub> are also volcanic gases, but the majority of the column density is atmospheric, especially with a relatively long pathlength as is the case here. The temperature of the gas ( $t_{gas}$ ) is extracted from the retrieval performed at the  $\nu_1 + \nu_3$  feature described in Section 3.1, on a spectrum-by-spectrum basis. The temperature associated with emission of radiation from the gas ( $t_{gasE}$ ), is left as a free parameter. This is because there will be hot gas which contributes primarily to



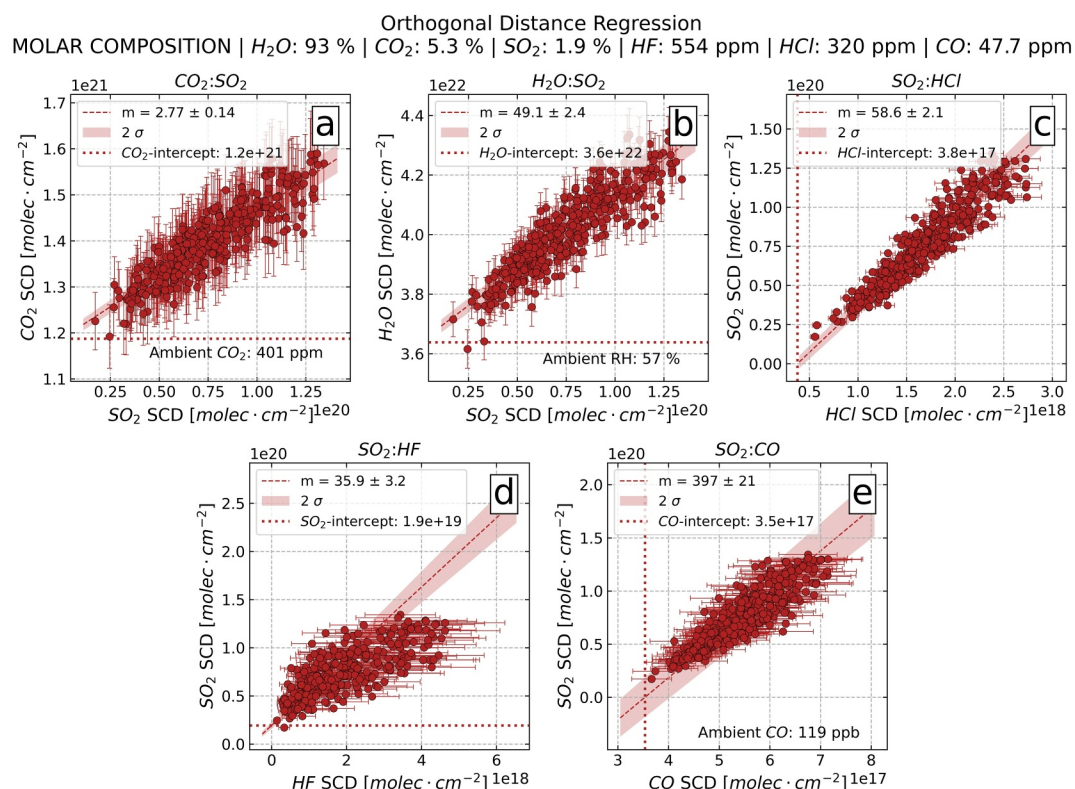


**Figure 4.** Plume composition measured at the vent by direct LOS FTIR measurements. Scatter plots of the measured SCDs for pairs of target gases. The dashed line is a linear fit to the data calculated using the Orthogonal Distance Regression (ODR) method, and yielding the molar ratio between the two species. The shaded area represents the 95% confidence interval on the regression. The fitting error on the  $SO_2$  SCD is generally  $<1\%$ , often smaller than the size of the data symbols on this plot. (a)  $CO_2/SO_2 = 2.77 \pm 0.14$ , derived ambient  $CO_2$  concentration is  $\sim 401$  ppm; (b)  $H_2O/SO_2 = 49.1 \pm 2.4$ , derived ambient relative humidity is  $\sim 57\%$ ; (c)  $SO_2/HCl = 58.6 \pm 2.1$ ; (d)  $SO_2/HF = 35.9 \pm 3.2$ ; (e)  $SO_2/CO = 397 \pm 21$ , ambient  $CO$  concentration is  $\sim 119$  ppb. The overall molar composition of the gas, derived using the ratios presented in this figure, is presented at the top.

emission in the  $\nu_1$   $SO_2$  band, and not to absorption, while the gas temperature retrieved in the  $\nu_1 + \nu_3$  window is only for the cooler absorbing gas layer. The ratio between the Planck functions of the gas and the source thus reflects the dynamic nature of the source and the fact that the FOV of the instrument is filled with hot incandescent material to varying degrees. Figure 5 shows an example fit in that window. We performed fits with a number of particulate species as external mixtures, including SA,  $H_2O$  droplets and silicate ash, and every combination of the three. The best fits were observed with a combination of SA and  $H_2O$  aerosols. The modeled spectra produce large aerosol optical depths, responsible for up to 50%–60% of the modeled extinction. This is consistent with visual observations of a heavily condensed plume, resulting from the high temperature contrast between a hot plume (350–650 K) and a relatively cold atmosphere (284 K). The measurement residual shows systematic misfits, notably at  $\sim 875$   $cm^{-1}$ , at  $\sim 1000$   $cm^{-1}$ , as well as around the  $SO_2$  doublet around 1250  $cm^{-1}$ . This suggests there is still some variability in the spectra which is unaccounted for by our simplified model. Likely explanations for those misfits are: (a) features in the emissivity of the source; (b) non-linearity of the IRF; and (c) inappropriate set of refractive indices for the aerosol species. This latter factor is addressed in Section 4.2 below.

We produce a time series of retrieved mass SCDs for both sulfate and water aerosols. Figure 6 summarizes the results of the aerosol retrieval for the entire data set, with individual datapoints colored according to the gas temperature retrieved in the  $\nu_1 + \nu_3$  window (see Section 3.1). For the first time, we can report measurements of the molar ratio between gaseous  $SO_2$  and sulfate in aqueous solution ( $SO_4^{2-}$  (aq)) with the concentration of this aerosol discussed in Section 4.4) from a direct LOS geometry with a highly dynamic high-temperature source of radiation (i.e., lava fountaining). The scatter plot of  $SO_2$  against  $SO_4^{2-}$  shows a strong correlation between the two species. The instantaneous molar ratio (ratio obtained from a single spectrum) fluctuates between 100 and 250,

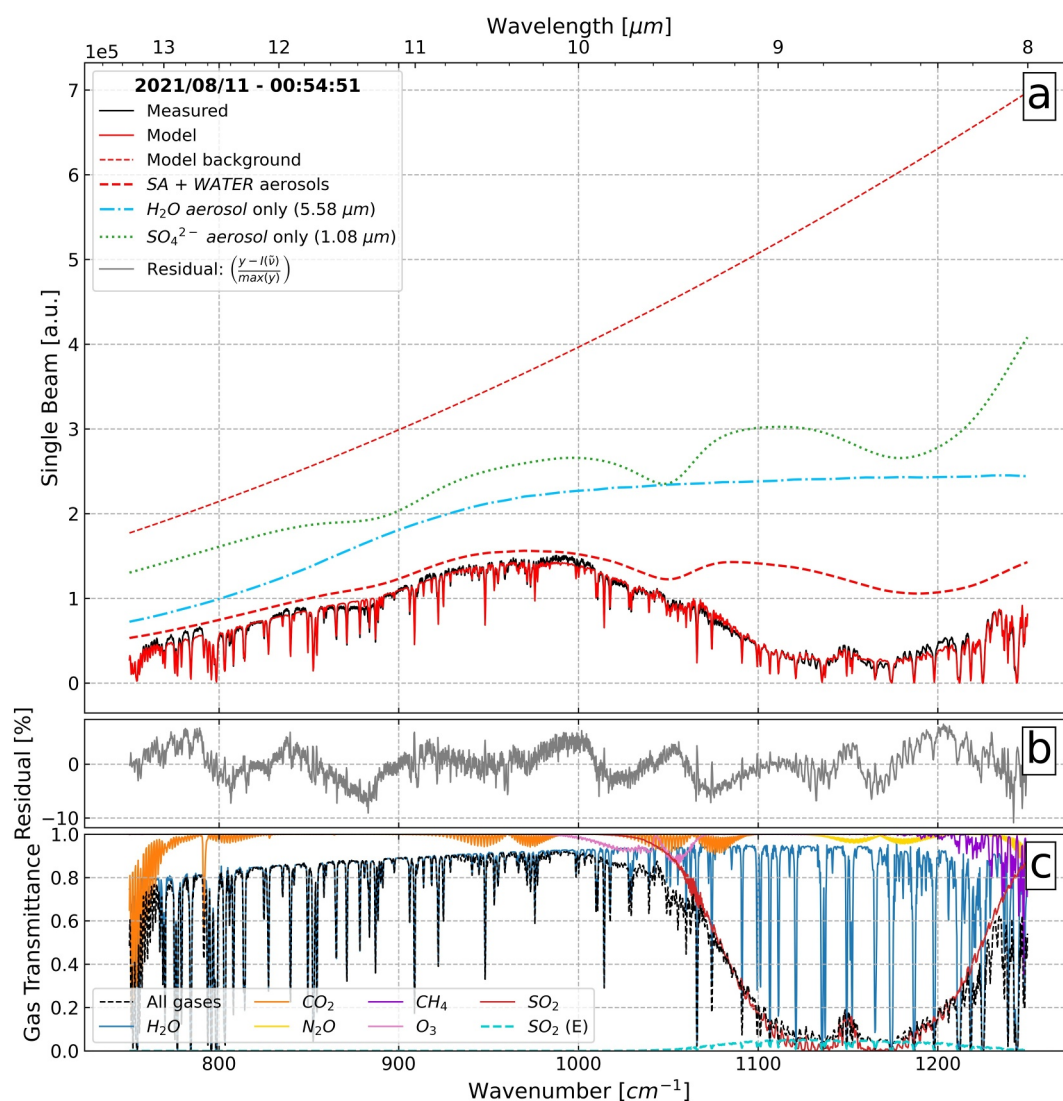


**Figure 5.** Detailed results of a fit performed over the TIR retrieval window on a single example spectrum. The retrieval was performed with a  $\text{H}_2\text{SO}_4$  concentration of 38 wt.% in the SA droplets, and the aerosol size for both SA and  $\text{H}_2\text{O}$  aerosol were left as free parameters. (a) Measured (black) and modeled (red) spectra. The modeled background is shown as a dashed red line. Also shown as dotted lines are partial forward models using the aerosol transmittances only:  $\text{SO}_4^{2-}$  aerosols in green,  $\text{H}_2\text{O}$  aerosols in blue, and the combination of both in red. (b) Measurement residual. (c) Modeled transmittances for individual gas species. The relative contribution of the emission term for  $\text{SO}_2$  is also shown.

with a mean value of  $160 \pm 49$ . When considering the cumulative values for both species over the course of the data set, the resulting ratio is  $169 \pm 25$ . Although the instantaneous ratio exhibits sharp variations, the data outline a well-defined relationship as shown in the scatter plot between  $\text{SO}_2$  and  $\text{SO}_4^{2-}$ . The ratio obtained by linear regression of these data has a higher value of  $241 \pm 8.6$ . This is reflected in the fact that the intercept for this linear regression is not zero, suggesting a secondary source for the sulfate aerosols besides the main vent outgassing, one with significantly lower  $\text{SO}_2$  gas content. Retrieved SA sizes range between 1.2 and 2.0  $\mu\text{m}$ , with a mean value of  $1.4 \pm 0.1 \mu\text{m}$ .

For water aerosols, the scatter plot between gas and aerosol SCDs shows a strong negative correlation between the two species. When corrected for background atmospheric  $\text{H}_2\text{O}$  (g) content, the ratios span a wide range of values (1–1000), with high temperature plumes showing a stronger partitioning toward the gas phase. Retrieved sizes for the water aerosol phase range between 2 and 10  $\mu\text{m}$ , with a mean value of  $6.3 \pm 1.2 \mu\text{m}$ .

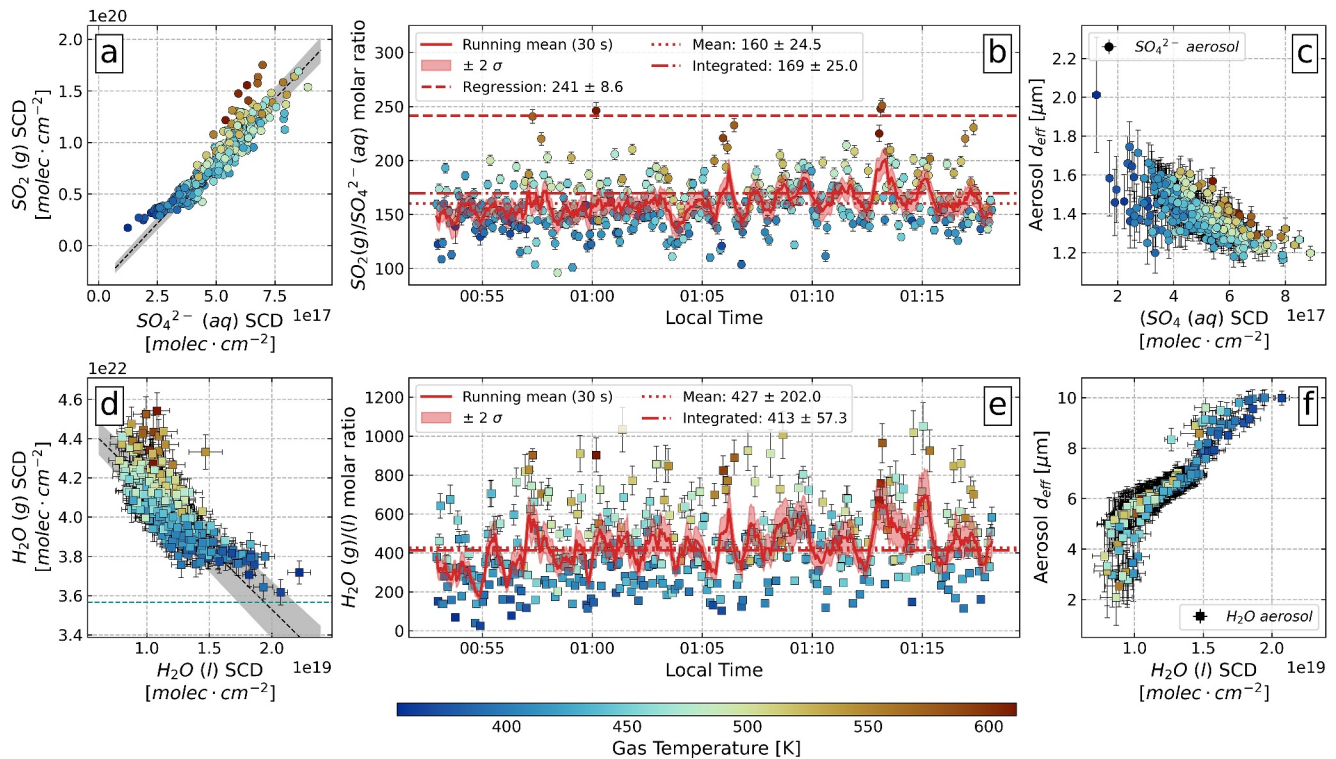


**Figure 6.** Aerosol composition for the 30 min data set. All data points are colored according to the gas temperature. (a)–(c) Sulfate aerosols. (a) Scatter plot of retrieved molecular SCD for  $\text{SO}_2(\text{g})$  against  $\text{SO}_4^{2-}(\text{aq})$ . An Orthogonal Distance Regression (dashed gray line and shaded area) yields a molar ratio of 241, with a significant non-zero intercept. (b) Time series of instantaneous  $\text{SO}_2/\text{SO}_4^{2-}$  molar ratios. The solid red line is a moving average for the data with the 95% confidence interval shown in shaded red. The overall ratios derived over the entire data set using three separate methods are shown as horizontal lines: (1) Orthogonal Distance Regression of the scatter data in the left panel:  $241 \pm 8.6$ ; (2) Mean instantaneous ratio:  $160 \pm 25$ ; and (3) An integrated ratio where we consider the total mass accumulated over the entire time series:  $169 \pm 25$ . (c) Scatter plot of the retrieved size of the sulfate aerosol against the retrieved SCD. (d)–(f) Water aerosols. (d) Scatter plot of retrieved molecular SCD for  $\text{H}_2\text{O}(\text{g})$  retrieved in the  $2020\text{--}2180\text{ cm}^{-1}$  window against  $\text{H}_2\text{O}(\text{l})$  aerosol retrieved in the TIR window. Also shown is the ambient  $\text{H}_2\text{O}$  SCD derived from the scatter plot between  $\text{SO}_2$  and  $\text{H}_2\text{O}$  in Figure 4 (blue horizontal dotted line). An Orthogonal Distance Regression to the data (dashed gray line and shaded area) shows a negative correlation. (e) Time series of instantaneous  $\text{H}_2\text{O}$  gas/aerosol ratios. Gas SCDs have been adjusted to subtract the ambient  $\text{H}_2\text{O}$  column. The solid red line is a moving average for the data with the 95% confidence interval shown in shaded red. The mean instantaneous ratio ( $427 \pm 202$ ) and integrated ratio ( $413 \pm 57$ ) are also shown as horizontal lines. (f) Scatter plot of the retrieved size of the water aerosol against the retrieved SCD.

## 4. Discussion

### 4.1. $\text{SO}_2$ Retrieved in Two Spectral Windows

Although not the most abundant gas in the plume,  $\text{SO}_2$  constitutes a reference for remote quantification of volcanic emissions, because of two important facts: (a) In the absence of anthropogenic pollution sources,  $\text{SO}_2$  is virtually absent from the background atmosphere, making its detection diagnostic of a volcanic source; and (b) the molecule presents a series of very distinctive spectral features which are relatively easy to model. In the IR range,  $\text{SO}_2$  presents 3 separate vibrational features: the  $\nu_1$  feature centered at  $1150\text{ cm}^{-1}$  ( $8.7\text{ }\mu\text{m}$ ), the  $\nu_3$  feature centered at  $1360\text{ cm}^{-1}$  ( $7.3\text{ }\mu\text{m}$ ), and the  $\nu_1 + \nu_3$  feature centered at  $2500\text{ cm}^{-1}$  ( $4\text{ }\mu\text{m}$ ). The  $\nu_1$  and  $\nu_3$  features at lower wavenumbers are routinely used for infrared satellite detection of  $\text{SO}_2$  (Campion et al., 2010; Carboni et al., 2016; Prata & Kerkmann, 2007; Realmuto et al., 1994), while the  $\nu_1 + \nu_3$  feature is the preferred method for quantification with OP-FTIR (Burton et al., 2007; Horrocks et al., 2001; Oppenheimer et al., 1998). Its relatively lower magnitude makes it more appropriate for quantifying high column densities, as is often the case in direct LOS geometries at close range. The  $\nu_3$  feature is generally not appropriate for use in the troposphere, as the high water vapor renders the atmosphere opaque at those wavenumbers, even over short pathlengths. However, the  $\nu_1$  feature is accessible, and indeed this strong  $\text{SO}_2$  band must be accounted for in the aerosol retrievals presented in this study. As a result, we obtain two separate quantifications for  $\text{SO}_2$  SCDs from the  $\nu_1$  and  $\nu_1 + \nu_3$  bands.

Figure 7 presents a comparison between the two retrieved quantities. In general,  $\text{SO}_2$  SCDs retrieved in the TIR window (i.e.,  $\nu_1$ ) along with the aerosols are systematically higher than those retrieved with the  $\nu_1 + \nu_3$  feature, by



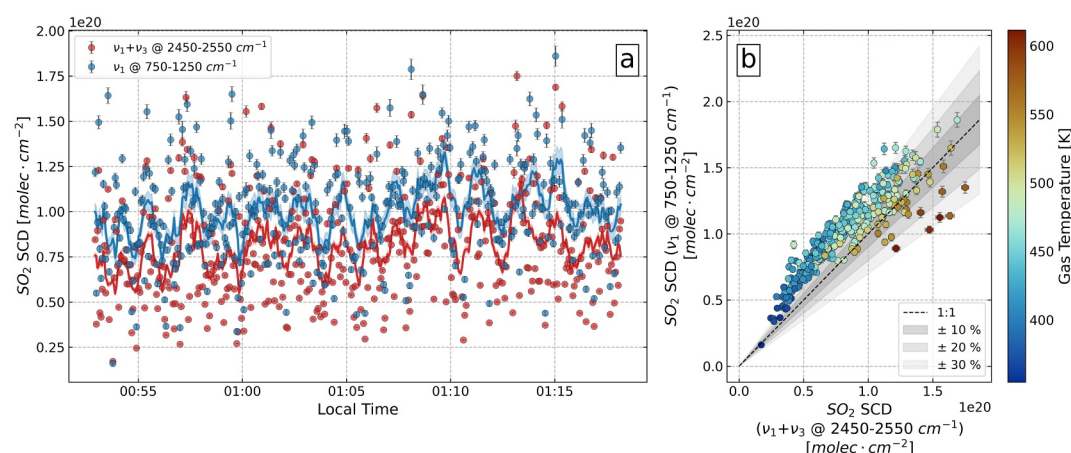


**Figure 7.** Comparison of  $\text{SO}_2$  SCDs retrieved in two spectral windows. (a) Time series of  $\text{SO}_2$  SCDs retrieved with the  $\nu_1$  feature (TIR window, red) and with the  $\nu_1 + \nu_3$  feature (2450–2550  $\text{cm}^{-1}$ , blue). Individual data points and their retrieval errors are plotted, as well as a running average with a window of 9 spectra ( $\sim 30$  s). (b) Scatter plot of the retrieved  $\text{SO}_2$  SCDs with both methods. Data points are colored according to the gas temperature retrieved in the  $\nu_1 + \nu_3$  window.

a factor of 50%–60%. This is the case, even when the gas temperature in the TIR fit is fixed as the same as in the  $\nu_1 + \nu_3$  fit. The  $\nu_1$  feature is much more sensitive to lower SCDs, and therefore more prone to saturation, especially in the higher range of concentrations observed in this study. This can be seen in the scatter plot (Figure 7b), where the  $\nu_1$  band overestimates the  $\text{SO}_2$  SCD at low temperatures, but underestimates it at very high temperatures. The presence of  $\text{SO}_4^{2-}$  aerosols, and the generally more complex nature of the background signal in the TIR window, also makes the retrieval more difficult. This discrepancy highlights the complexity of the radiative transfer problem in the TIR range, and further supports the case for using the  $\nu_1 + \nu_3$  feature wherever possible for the most accurate retrieval of  $\text{SO}_2$ .

#### 4.2. Accurate Determination of Gas Temperature

The strength of a given absorption line for gases depends in part on the temperature of the gas. This temperature dependence is different for each gas and for each individual line. In a dynamic volcanic plume environment (as studied here) the temperature will fluctuate strongly (100s K) on the timescale between individual measurements due to variable mixing of hot gas with cold atmosphere. Therefore, variable degrees of error will be introduced when erroneously assuming a single gas temperature for all measured spectra if, in reality, the gas temperature is changing. This will affect the measured gas ratios in different ways. Figure 8 presents a series of scatter plots for selected pairs of gases, and the resulting molar ratios derived over the entire data set assuming a series of increasing single gas temperatures. The ratios obtained using a variable temperature fitted with the  $\nu_1 + \nu_3$   $\text{SO}_2$  feature are also shown. The effect of gas temperature is most pronounced on the  $\text{SO}_2$  SCD, but affects other gases to various degrees, leading to variations in each ratio that often exceed the fitting uncertainty. The magnitude of this effect is different for each ratio, and will lead to variations in the retrieved gas composition. Therefore, care must be taken when interpreting changes in molar ratios derived from OP-FTIR data, particularly when associated with erupting lavas with highly variable gas temperatures. The two most recent studies on the Fagradalsfjall eruption present OP-FTIR (Halldórsson et al., 2022; Scott et al., 2023) derived gas ratios from measurements during fountaining phases, assuming a single temperature for the volcanic gases, as low as 280 K in Scott et al. (2023). As illustrated here, determining a representative temperature is difficult, and will depend on many factors including ambient atmospheric conditions and the nature of the gas emissions. Therefore, variations in the measured ratios may reflect changes in the thermal profile of the plume, rather than changes in the gas composition. We address this issue here by quantifying the magmatic gas temperature for each individual spectrum, in a manner similar to that used by La Spina et al. (2015) on lava fountaining events at Mt. Etna in 2001.

The retrieval of aerosol column density is, strictly speaking, not temperature-dependent, as the extinction is modeled based on Mie scattering principles and refractive indices measured at a temperature of 298 K (Lund Myhre et al., 2003). This approach is based on the assumption that the aerosols tend to form in the cooler parts of the plume, where the temperature is closer to atmospheric temperature. However, inaccurate temperature

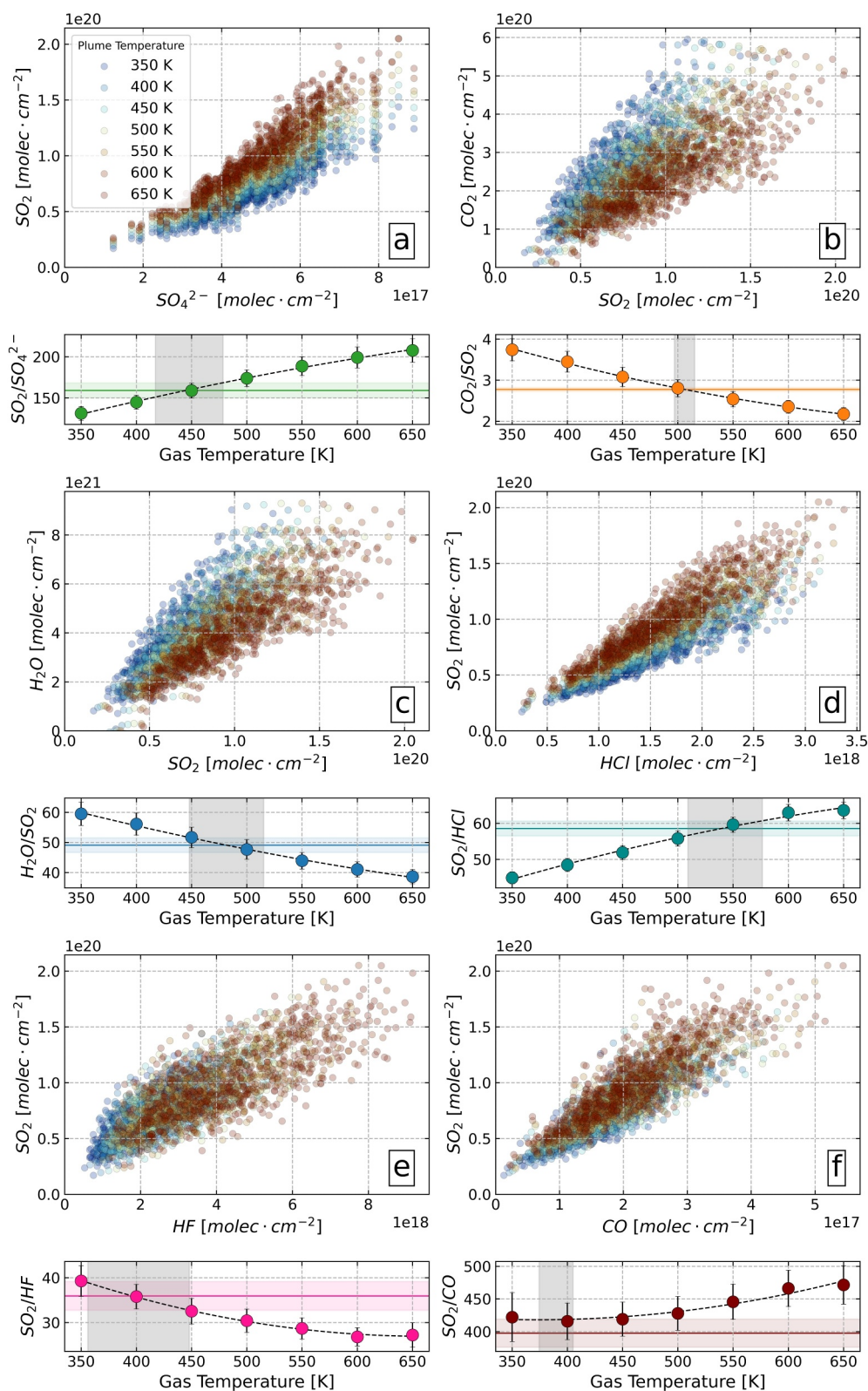


Figure 8.



estimates for the  $\text{SO}_2$  gas still result in significant errors on the  $\text{SO}_2/\text{SO}_4^{2-}$  ratios. Mean  $\text{SO}_2/\text{SO}_4^{2-}$  ratios vary between 131 and 208, with higher ratios when assuming higher gas temperatures. Similar effects may be expected when assuming a single temperature for the atmospheric gas (i.e.,  $\text{CO}_2$  and  $\text{H}_2\text{O}$ ). However, we found that the magnitude of the error introduced by assuming a single atmospheric temperature is negligible when compared to the errors associated with plume gas temperature discussed above (see details in Supporting Information S1).

When properly addressed, temperature-corrected analysis produces a more representative range of ratios. This methodology is therefore necessary in order to investigate aerosol formation mechanisms and their dependence on temperature in any detail. It should be noted that the determination of a single temperature for each individual measurement of the gas plume is an oversimplification of the thermal profile along the line of sight (see Figure 1). At the point of emission, gas is released at the eruptive temperature, after which entrainment of ambient air creates a steep temperature (and concentration) gradient away from the radiation source. The assumption of a single temperature will therefore introduce errors on both temperature and retrieved SCD but is unavoidable without further independent constraints on the temperature profile along the line of sight.

### 4.3. Aerosol Formation at the Vent

Primary sulfate aerosols (i.e., those originating from the hot magmatic gases) have been observed in near-source volcanic plumes at numerous volcanoes, and sampled for a number of eruptions: for example, Kīlauea (Kroll et al., 2015; Naughton et al., 1975), Masaya (Allen et al., 2002; De Moor et al., 2013; Mather et al., 2003), Lascar (Mather et al., 2004; Menard et al., 2014), Erta Ale (De Moor et al., 2013), Etna (Roberts et al., 2018), Villarica (Mather et al., 2004), Eyjafjallajökull in both fissure and the more explosive summit phase (Ilyinskaya et al., 2012) and Holuhraun (Ilyinskaya et al., 2017). A commonly proposed mechanism for primary sulfate aerosol formation in very young plumes starts with the oxidation of  $\text{SO}_2$  into  $\text{SO}_3$  by atmospheric oxygen at high temperatures, followed by reaction with  $\text{H}_2\text{O}$  to form gaseous  $\text{H}_2\text{SO}_4$  (Allen et al., 2002; Cadle et al., 1971; Mather et al., 2006; Roberts et al., 2019). The hygroscopic  $\text{H}_2\text{SO}_4$  (g) is then quickly converted into aqueous sulfate aerosol. The limiting reaction in this chain is the initial oxidation of  $\text{SO}_2$  to  $\text{SO}_3$ , which is highly endothermic - and thus mainly occurs at high temperatures of  $>800$  K within the first seconds of the plume lifetime. Reported values for the  $\text{SO}_2/\text{SO}_4^{2-}$  molar ratio at different volcanoes span a wide range of values, from as low as 2 at Soufrière Hills volcano, Montserrat (Allen et al., 2000) to as high as 50,000 from Eyjafjallajökull (Ilyinskaya et al., 2012). They are at least in part controlled by the type of eruption, which defines the physical and chemical conditions for  $\text{SO}_3$  production. Roberts et al. (2019) argue that the observed ratios cannot be explained by equilibrium chemistry, and are instead limited by reaction kinetics and availability of oxidants during plume mixing with the atmosphere, both of which would depend on the manner in which outgassing occurs. For example, in dome eruptions, where high-temperature interactions between volcanic and atmospheric gases may be enhanced by air circulation within a porous dome,  $\text{SO}_2/\text{SO}_4^{2-}$  ratios are markedly low: 2 at Montserrat (Allen et al., 2000) and 2.33 at Bezymianny (Zelenski et al., 2015). On the other hand, more violent eruptions, such as fire fountaining, result in much higher values (Ilyinskaya et al., 2012), perhaps because explosive activity and an associated stronger gas flow out of the volcanic vent and turbulent mixing favor more rapid cooling of the gas during release thus reducing the extent of  $\text{SO}_2$  reactions with atmospheric oxidants. The range of  $\text{SO}_2/\text{SO}_4^{2-}$  ratios presented here (100–250) are consistent with those previously reported for other open-vent basaltic eruptions: for example, Holuhraun (100–1000; Ilyinskaya et al., 2017), Kīlauea (10–1000; Naughton et al., 1975; Kroll et al., 2015).

The time series of instantaneous  $\text{SO}_2/\text{SO}_4^{2-}$  ratios (Figure 6b) shows considerable variability from spectrum to spectrum. This variability is partially explained by the fluctuations in gas temperature. Figure 9 presents the relationship between a series of aerosol characteristics and the fitted gas temperature. This temperature is an oversimplification of the integrated gas temperature along the line of sight, but it is well correlated with the  $\text{SO}_2$  SCD, and thus can be regarded as a proxy for the average plume age dominating the field of view - younger

**Figure 8.** Effect of assumed gas temperature on the retrieved molar ratios. For each ratio, the scatter plot is presented in the top panel, colored according to the assumed gas temperature. (a)  $\text{SO}_2/\text{SO}_4^{2-}$ ; (b)  $\text{CO}_2/\text{SO}_2$ ; (c)  $\text{H}_2\text{O}/\text{SO}_2$ ; (d)  $\text{HCl}/\text{SO}_2$ ; (e)  $\text{HF}/\text{SO}_2$ ; (f)  $\text{CO}/\text{SO}_2$ . The bottom panel presents the retrieved ratios and associated fitting uncertainty ( $2\sigma$ ) against the assumed temperature. The ratio derived using the fitted gas temperature is presented as a horizontal line, with a shaded area in the corresponding color representing the fitting uncertainty. The shaded gray area represents the range of temperatures that would produce a ratio similar to that obtained with a variable temperature (within the uncertainty). Ratios are calculated as the slope of the linear regression to the scatter, except in the case of  $\text{SO}_2/\text{SO}_4^{2-}$ , where the ratio is the mean of all individual ratios.

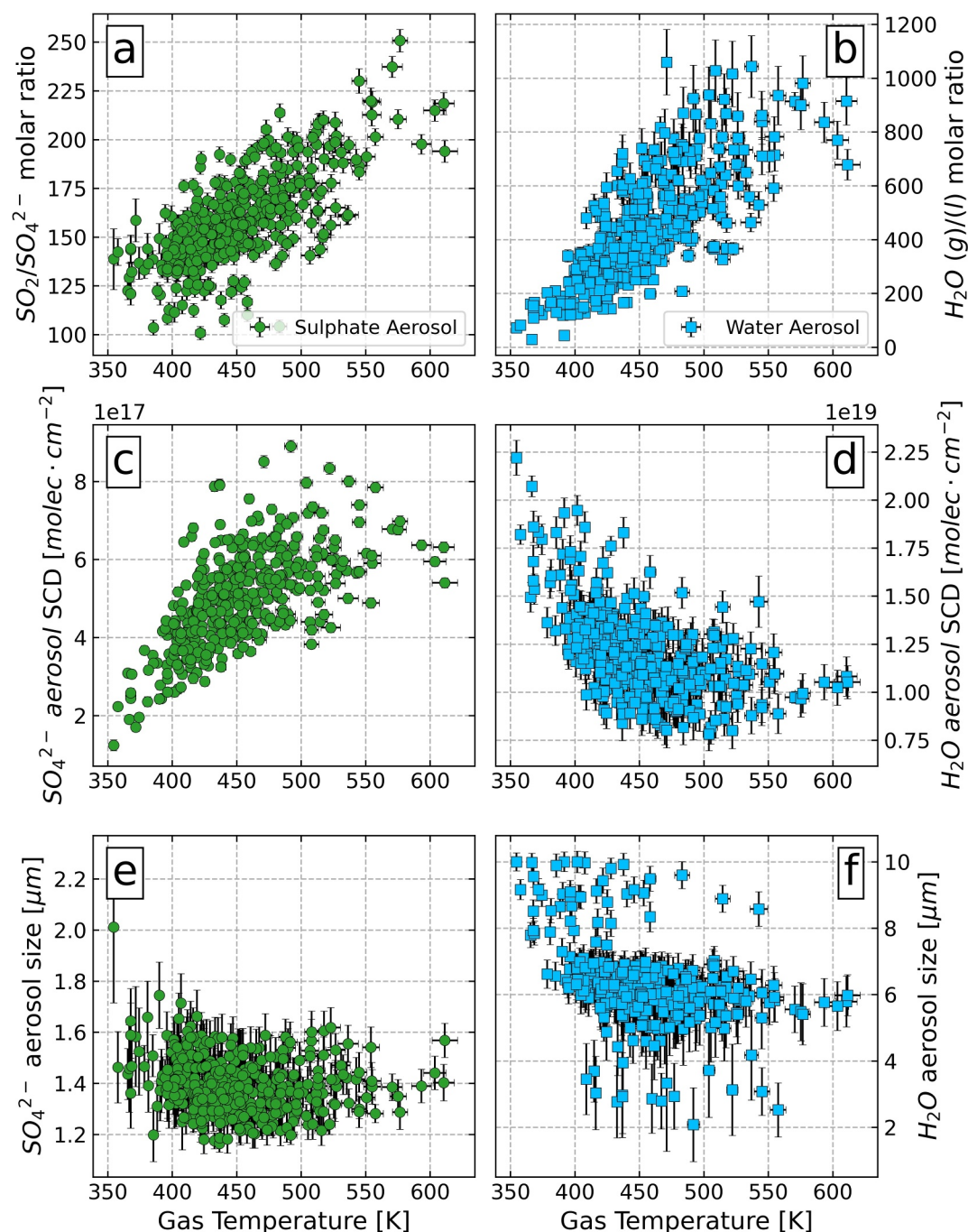


**Figure 9.** Scatter plots of retrieved parameters against fitted gas temperature for sulfate aerosols (left, green circles) and water aerosols (right, blue squares). (a)  $\text{SO}_2/\text{SO}_4^{2-}$  molar ratio. (b)  $\text{H}_2\text{O}$  gas/aerosol ratio. (c) Retrieved  $\text{SO}_4^{2-}$  aerosol SCD. (d) Retrieved  $\text{H}_2\text{O}$  aerosol SCD. (e) SA particle size. (f)  $\text{H}_2\text{O}$  aerosol particle size.

plumes being hotter and more concentrated, and slightly older plumes being colder and more dilute given the rapid cooling and mixing that occurs once magmatic gases have been released into the background atmosphere. The decrease in gas/aerosol ratios related to lower retrieved gas temperatures for both the sulfate and water aerosols (Figure 9a and 9b), suggests that we are capturing the condensation of aerosols from the gas phase as the plume rapidly cools down. Since the only source of sulfur in the plume is volcanic, we would predict that hotter, more concentrated plumes will have higher column amounts of both  $\text{SO}_2$  and SA. This is indeed what we observe with hotter plumes generally associated with higher amounts of SA (Figure 9c), reflecting the genetic relationship

between SO<sub>2</sub> and SA. Water aerosols, however, increase in abundance with decreasing temperature (Figure 9d). This suggests that they condense from both volcanic and atmospheric sources of H<sub>2</sub>O (g) as the plume is diluted and cooled. It is also possible that SA might condense water vapor into it and grow and dilute to have spectral qualities that are more like water droplets and so are retrieved as such. We note that the consideration of multiple scattering effects may alter our findings, especially given the large optical thicknesses measured here. This has been identified as an area for improvement and will be the subject of future work.

The size of the SA droplets remains very similar, regardless of plume temperature, except in the case of plumes <400 K, where slightly larger droplets can be observed (Figure 9f). The size of the water aerosol, on the other hand, broadly increases as the temperature decreases, with droplets as large as 10 μm in diameter in the colder plumes (Figure 9e). The high-temperature data points represent a very hot plume, where the condensation of H<sub>2</sub>SO<sub>4</sub> has only partially occurred, and water aerosols are essentially absent. Data points with colder gas temperatures capture a more mature plume, where both H<sub>2</sub>SO<sub>4</sub> and H<sub>2</sub>O have fully condensed.

#### 4.4. Composition of the Sulfate Aerosol (SA) Droplets

The spectral shape of the extinction coefficient for SA is dependent on both the chemical composition of the droplets and the particle size (Sellitto & Legras, 2016; Smekens et al., 2023). The relative effect of a change in particle size is much more pronounced than a change in composition, and therefore we have opted to leave particle size as a free parameter in the retrieval, while fixing composition, in a manner similar to the approach used by Smekens et al. (2023) for emission measurements. However, there are some subtle changes due to composition that may affect the quality of the fits. Acidity of the SA droplets is defined as the weight fraction of H<sub>2</sub>SO<sub>4</sub> in the solution. We used refractive indices from Lund Myhre et al. (2003), which range in acidity from 38 to 81 wt.% H<sub>2</sub>SO<sub>4</sub> at 298 K. Observations of a significant dip in the measured spectra at ~875 cm<sup>-1</sup>, and the presence of systematic misfits in the measurement residual at those frequencies, suggest an overall aerosol composition with very low acidity, as the position of the spectral peaks in the SA cross section generally shifts toward lower wavenumbers with decreasing acidity. This is counter to the expectation for highly acidic sulfate aerosols at the time of initial condensation and measurements in some near-source plumes (e.g., Mather et al., 2003). However, using a single aerosol phase with acidity greater or equal to 38 wt.%, the lowest value in the data set from Lund Myhre et al. (2003), fails to accurately reproduce the observed absorptions, and generally produces poorer quality fits. Therefore, we have modeled the aerosol phase as an external mixture of SA with a concentration of 38 wt. % H<sub>2</sub>SO<sub>4</sub> and H<sub>2</sub>O aerosols. We can reasonably expect that the aerosol phase will co-nucleate or eventually coalesce over time to produce a single concentration. We have retrieved these two end-member aerosol (SA and water droplets) in order to allow us to account for the variable timescales of such processes, which may, at least under some circumstances, occur over timescales much longer than the age of the observed plumes here (in some cases only a few seconds). Further improvements to the method may be gained by considering a single SA phase with variable acidity, or aerosol droplets with an acid core and a diluted shell, both of which may be more representative of the physical reality within the plume.

#### 4.5. Temporal Trends

Although the data set presented here only captures a short period of ~30 min, the data show that it is possible to pick out some subtle temporal variations using this method. Figure 10 presents time series of various measured quantities and ratios. Between the start and end of the measurement period, there was an increase in the intensity of degassing behavior and enhanced effusion rate noted via visual observations. This was reflected in gradual changes for several parameters within our data set. In order to visually emphasize the longer period variations within the signals, the parameters derived from OP-FTIR data are presented as running averages with a moving window of 9 data points (~30 s), and a linear regression is fitted to the time series to reveal overall increases or decreases over the course of the measurements. The measured peak intensity of the FTIR spectrum, as well as the gas temperature, increase over time. The retrieved SO<sub>2</sub> SCDs increase as well. This reflects the overall increase in the intensity of the activity (and the magnitude of the outgassing) at the surface. As the intensity of the bubbling at the lava surface increases, the observed gas plumes are increasingly hotter and younger, which is reflected by the increase in measured ratios between gas and aerosol phase for both sulfate and water. This increased degassing intensity might also change the dynamics of air mixing into the hot volcanic environment reducing the oxidation of SO<sub>2</sub> to form SA. Finally, the CO<sub>2</sub>/SO<sub>2</sub> ratio increases, while the SO<sub>2</sub>/HCl ratio decreases. The magnitudes of these ratio changes are very small, and not likely to represent a significant change in the source of the gas.

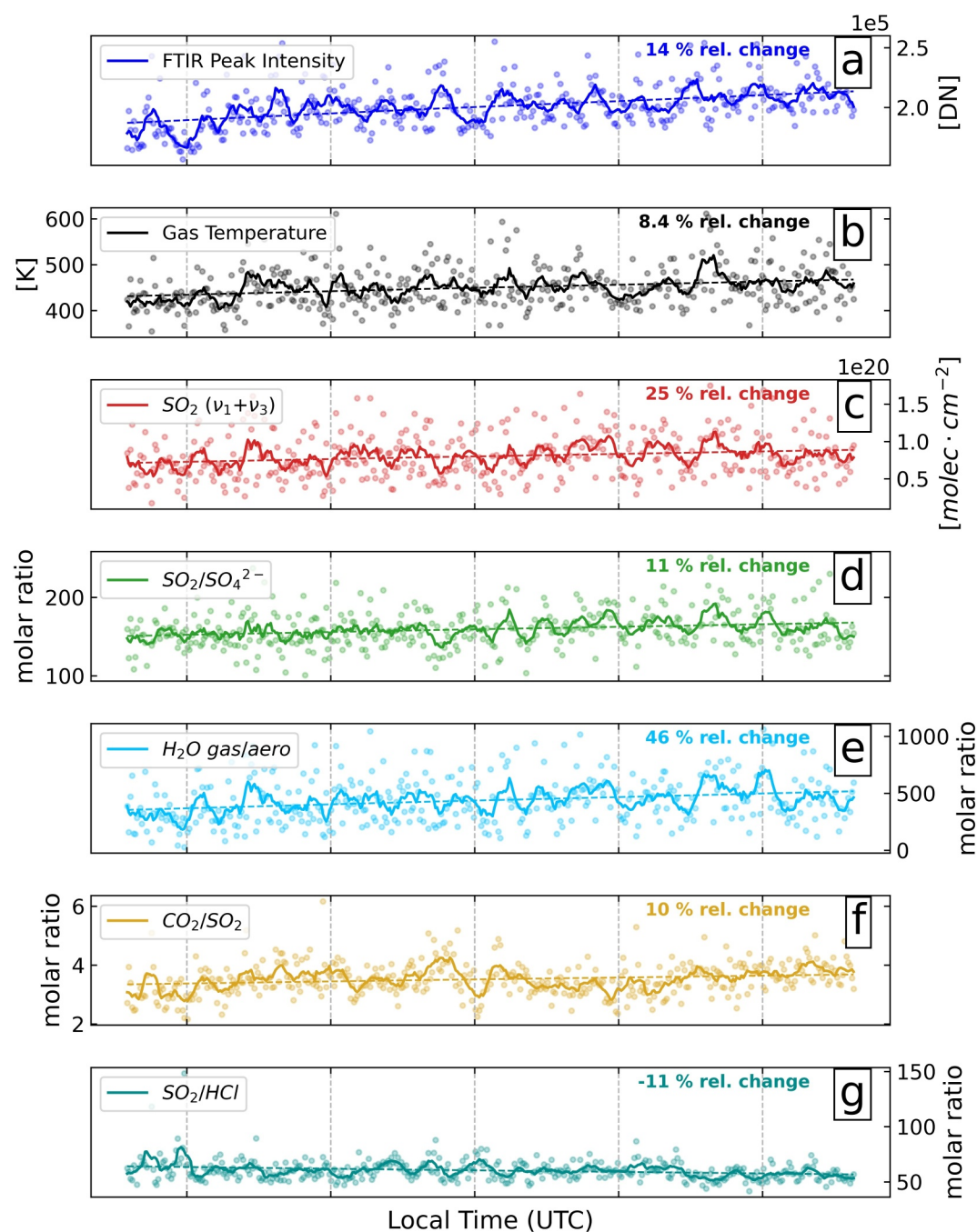


**Figure 10.** Time series of various quantities over the data set: (a) FTIR spectrum peak intensity (blue, in digital number or DN); (b) gas temperature (black, in K); (c)  $\text{SO}_2$  SCD (red in  $\text{molec} \cdot \text{cm}^{-2}$ ); (d)  $\text{SO}_2/\text{SO}_4^{2-}$  molar ratio (green); (e)  $\text{H}_2\text{O}$  gas/aerosol molar ratio (light blue); (f)  $\text{CO}_2/\text{SO}_2$  molar ratio (yellow); and (g)  $\text{SO}_2/\text{HCl}$  molar ratio (teal). Circles are individual data points. Running averages of the chosen parameter ( $\sim 30$  s moving window) are shown as a solid line. A linear regression (dashed line) is also fitted to the data, in order to emphasize the general trend over time. The relative change over the course of the data set with respect to the value at the start is also indicated.

Nevertheless, they may reflect some level of fractionation of the gas between the main erupting vent and the effusive activity and subtle changes in the balance between the concentrations of these different components in the spectrometer's line of sight. However, without systematic quantification of the composition of lava flow degassing and background contributions from sources such as sea spray aerosol, it is challenging to definitively discuss the expected effects of mixing different proportions of these end-members into the main plume.



## 5. Conclusions

We present a new method for retrieving quantitative information about primary aerosols in volcanic plumes from direct line-of-sight OP-FTIR measurements. Although accurate quantification of the  $\text{SO}_2/\text{SO}_4^{2-}$  ratio requires a careful consideration of the thermal complexity present in the viewing geometry, we show that it is possible to retrieve quantitative information from uncalibrated spectra in the TIR window. Plume temperatures evaluated using the  $\nu_1 + \nu_3$  spectral feature of  $\text{SO}_2$  show a range of 350–650 K. The overall gas composition (93%  $\text{H}_2\text{O}$ ; 5.3%  $\text{CO}_2$ ; 1.9%  $\text{SO}_2$ , 554 ppm HCl, 320 ppm HF, 48 ppm CO) does not exhibit significant variability over the course of our measurements. However, we report a temperature-dependent  $\text{SO}_2/\text{SO}_4^{2-}$  ratio ranging from 100 to 250, with higher-temperature plumes exhibiting higher ratios. Changes in the measured ratio occur on timescales of only a few minutes, and are linked with observable changes in the intensity of the degassing. In parallel to the changes in S speciation, we observe the rapid condensation of water droplets as the plume cools down, with  $\text{H}_2\text{O}$  gas/aerosol ratios going from 1000 in hot plumes to  $<1$  in the coldest plumes. Our results suggest a previously untapped potential contained in OP-FTIR spectra of magmatic gases, and that these data may be used to investigate high-temperature formation of sulfate aerosols for various eruptive styles and magma compositions. It is also possible to extend the retrieval to include ash for more explosive fountaining events, as the original algorithm (Smekens et al., 2023) was designed mainly to retrieve ash column densities. Although there remain significant barriers to deploying OP-FTIR as a continuously operating automated monitoring tool (e.g., instrument fragility and cost, availability of power at the measurement site, changes in measurement geometry), our study shows the potential for such measurements to provide additional information. With the proper automation and in certain specific situations (i.e., a long-lasting eruption from fixed eruptive vents), the method could be used as a monitoring tool to provide real-time measurements of  $\text{SO}_2/\text{SO}_4^{2-}$  ratios at the point of emission during volcanic eruptions, which is an important parameter for air quality models. The method can also provide new insights into the variable degassing dynamics over the course of an eruption and their relationship to aerosol nucleation and microphysics.

## Data Availability Statement

Both the software and data presented in this manuscript are available in open access. The code used for the retrieval of column densities is available on Zenodo (Smekens, 2024) under a Creative Commons Attributions license. The data necessary to reproduce the figures have been archived with the Oxford University Research Archive (Smekens et al., 2024).

## Acknowledgments

The work outlined in this manuscript was supported by NERC awards NE/S004025/1 and NE/S004106/1. The authors would like to thank the staff at the Icelandic Meteorological Office for providing guidance during field measurements and facilitating access to the eruption site. We would also like to thank the staff at the NERC Field Spectroscopy Facility, who provided the OP-FTIR spectrometer used for this study. Finally, we thank Patrick Allard and an anonymous reviewer, as well as the editor, for their feedback and helpful suggestions on the manuscript.

## References

- Aiuppa, A., Burton, M., Calabiano, T., Giudice, G., Guerrieri, S., Liuzzo, M., et al. (2010). Unusually large magmatic  $\text{CO}_2$  gas emissions prior to a basaltic paroxysm. *Geophysical Research Letters*, 37(17). <https://doi.org/10.1029/2010GL043837>
- Aiuppa, A., Federico, C., Giudice, G., Guffrida, G., Guida, R., Gurrieri, S., et al. (2009). The 2007 eruption of Stromboli volcano: Insights from real-time measurement of the volcanic gas plume  $\text{CO}_2/\text{SO}_2$  ratio. *Journal of Volcanology and Geothermal Research*, 182(3–4), 221–230. <https://doi.org/10.1016/j.jvolgeores.2008.09.013>
- Allard, P., Burton, M., & Muré, F. (2005). Spectroscopic evidence for a lava fountain driven by previously accumulated magmatic gas. *Nature*, 433(7024), 407–410. <https://doi.org/10.1038/nature03246>
- Allard, P., Burton, M., Sawyer, G., & Bani, P. (2016). Degassing dynamics of basaltic lava lake at a top-ranking volatile emitter: Ambrym volcano, Vanuatu arc. *Earth and Planetary Science Letters*, 448, 69–80. <https://doi.org/10.1016/j.epsl.2016.05.014>
- Allen, A. G., Baxter, P. J., & Ottley, C. J. (2000). Gas and particle emissions from Soufrière Hills volcano, Montserrat, west Indies: Characterization and health hazard assessment. *Bulletin of Volcanology*, 62(1), 8–19. <https://doi.org/10.1007/s004450050287>
- Allen, A. G., Oppenheimer, C., Ferm, M., Baxter, P. J., Horrocks, L. A., Galle, B., et al. (2002). Primary sulfate aerosol and associated emissions from Masaya Volcano, Nicaragua. *Journal of Geophysical Research*, 107(D23), 5–8. <https://doi.org/10.1029/2002JD002120>
- Barsotti, S., Parks, M. M., Pfeffer, M. A., Óladóttir, B. A., Barnie, T., Titos, M. M., et al. (2023). The eruption in Fagradalsfjall (2021, Iceland): How the operational monitoring and the volcanic hazard assessment contributed to its safe access. *Natural Hazards*, 116(3), 3063–3092. <https://doi.org/10.1007/s11069-022-05798-7>
- Beirle, S., Hörmann, C., Penning De Vries, M., Dörner, S., Kern, C., & Wagner, T. (2014). Estimating the volcanic emission rate and atmospheric lifetime of  $\text{SO}_2$  from space: A case study for Kīlauea volcano, Hawai‘i. *Atmospheric Chemistry and Physics*, 14(16), 8309–8322. <https://doi.org/10.5194/acp-14-8309-2014>
- Borsdorff, T., Aan de Brugh, J., Hu, H., Aben, I., Hasekamp, O., & Landgraf, J. (2018). Measuring carbon monoxide with TROPOMI: First results and a comparison with ECMWF-IFS analysis data. *Geophysical Research Letters*, 45(6), 2826–2832. <https://doi.org/10.1002/2018GL077045>
- Burton, M., Pardo Cofrades, A., Hartley, M., Romero, J. E., Waters, E., Stewart, A. G., et al. (2023). Exceptional eruptive  $\text{CO}_2$  emissions from intra-plate alkaline magmatism in the Canary volcanic archipelago. *Commun. Earth Environ.*, 4(1), 467. <https://doi.org/10.1038/s43247-023-01103-x>
- Burton, M. R., Allard, P., Mure, F., & La Spina, A. (2007). Magmatic gas composition reveals the source depth of slug-driven strombolian explosive activity. *Science*, 317(5835), 227–230. <https://doi.org/10.1126/science.1141900>



- Burton, M. R., Oppenheimer, C., Horrocks, L. A., & Francis, P. W. (2001). Diurnal changes in volcanic plume chemistry observed by lunar and solar occultation spectroscopy. *Geophysical Research Letters*, 28(5), 843–846. <https://doi.org/10.1029/2000GL008499>
- Burton, M. R., Oppenheimer, C., Horrocks, L. A., & Francis, P. W. (2000). Remote sensing of CO<sub>2</sub> and H<sub>2</sub>O emission rates from Masaya volcano, Nicaragua. *Geology*, 28(10), 915–918. [https://doi.org/10.1130/0091-7613\(2000\)28<915:RSOAH>2.0.CO](https://doi.org/10.1130/0091-7613(2000)28<915:RSOAH>2.0.CO)
- Businger, S., Huff, R., Pattantyus, A., Horton, K., Sutton, A. J., Elias, T., & Cherubini, T. (2015). Observing and forecasting vog dispersion from Kilauea volcano, Hawaii. *Bulletin of the American Meteorological Society*, 96(10), 1667–1686. <https://doi.org/10.1175/BAMS-D-14-00150.1>
- Butz, A., Dinger, A. S., Bobrowski, N., Kostinek, J., Fieber, L., Fischerkeller, C., et al. (2017). Remote sensing of volcanic CO<sub>2</sub>, HF, HCl, SO<sub>2</sub>, and BrO in the downwind plume of Mt. Etna. *Atmospheric Measurement Techniques*, 10, 1–14. <https://doi.org/10.5194/amt-10-1-2017>
- Cadle, R. D., Wartburg, A. F., & Grahek, P. E. (1971). The proportion of sulfate to sulfur dioxide in Kilauea Volcano fume. *Geochimica et Cosmochimica Acta*, 35(5), 503–507. [https://doi.org/10.1016/0016-7037\(71\)90046-9](https://doi.org/10.1016/0016-7037(71)90046-9)
- Campion, R., Salerno, G. G., Coheur, P.-F. F., Hurtmans, D., Clarisse, L., Kazahaya, K., et al. (2010). Measuring volcanic degassing of SO<sub>2</sub> in the lower troposphere with ASTER band ratios. *Journal of Volcanology and Geothermal Research*, 194(1–3), 42–54. <https://doi.org/10.1016/j.jvolgeores.2010.04.010>
- Carbani, E., Grainger, R. G., Mather, T. A., Pyle, D. M., Thomas, G. E., Siddans, R., et al. (2016). The vertical distribution of volcanic SO<sub>2</sub> plumes measured by IASI. *Atmospheric Chemistry and Physics*, 16(7), 4343–4367. <https://doi.org/10.5194/acp-16-4343-2016>
- Carlsen, H. K., Ilyinskaya, E., Baxter, P. J., Schmidt, A., Thorsteinsson, T., Pfeffer, M. A., et al. (2021). Increased respiratory morbidity associated with exposure to a mature volcanic plume from a large Icelandic fissure eruption. *Nature Communications*, 12(1), 2161. <https://doi.org/10.1038/s41467-021-22432-5>
- De Moor, J. M., Fischer, T. P., Sharp, Z. D., King, P. L., Wilke, M., Botcharnikov, R. E., et al. (2013). Sulfur degassing at Erta Ale (Ethiopia) and Masaya (Nicaragua) volcanoes: Implications for degassing processes and oxygen fugacities of basaltic systems. *Geochemistry, Geophysics, Geosystems*, 14(10), 4076–4108. <https://doi.org/10.1002/ggge.20255>
- Dudhia, A. (2017). The reference forward model (RFM). *Journal of Quantitative Spectroscopy and Radiative Transfer*, 186, 243–253. <https://doi.org/10.1016/j.jqsrt.2016.06.018>
- Duffell, H., Oppenheimer, C., & Burton, M. (2001). Volcanic gas emission rates measured by solar occultation spectroscopy. *Geophysical Research Letters*, 28(16), 3131–3134. <https://doi.org/10.1029/2000GL012425>
- Francis, P., Burton, M. R., & Oppenheimer, C. (1998). Remote measurements of volcanic gas compositions by solar occultation spectroscopy. *Nature*, 396(6711), 567–570. <https://doi.org/10.1038/25115>
- George, M., Clerbaux, C., Bouarar, I., Coheur, P.-F., Deeter, M. N., Edwards, D. P., et al. (2015). An examination of the long-term CO records from MOPITT and IASI: Comparison of retrieval methodology. *Atmospheric Measurement Techniques*, 8(10), 4313–4328. <https://doi.org/10.5194/amt-8-4313-2015>
- Gordon, I. E., Rothman, L. S., Hargreaves, R. J., Hashemi, R., Karlovets, E. V., Skinner, F. M., et al. (2022). The HITRAN2020 molecular spectroscopic database. *Journal of Quantitative Spectroscopy and Radiative Transfer*, 277, 107949. <https://doi.org/10.1016/j.jqsrt.2021.107949>
- Greenfield, T., Winder, T., Rawlinson, N., MacLennan, J., White, R. S., Ágústssdóttir, T., et al. (2022). Deep long period seismicity preceding and during the 2021 Fagradalsfjall eruption, Iceland. *Bulletin of Volcanology*, 84(12), 101. <https://doi.org/10.1007/s00445-022-01603-2>
- Gudmundsson, G. (2011). Respiratory health effects of volcanic ash with special reference to Iceland. A review: Respiratory health effects of volcanic ash. *The Clinical Researcher J.*, 5(1), 2–9. <https://doi.org/10.1111/j.1752-699X.2010.00231.x>
- Halldórsson, S. A., Marshall, E. W., Caracciolo, A., Matthews, S., Bali, E., Rasmussen, M. B., et al. (2022). Rapid shifting of a deep magmatic source at Fagradalsfjall volcano, Iceland. *Nature*, 609(7927), 529–534. <https://doi.org/10.1038/s41586-022-04981-x>
- Horrocks, L., Burton, M., Francis, P., & Oppenheimer, C. (1999). Stable gas plume composition measured by OP-FTIR spectroscopy at Masaya Volcano, Nicaragua, 1998–1999. *Geophysical Research Letters*, 26(23), 3497–3500. <https://doi.org/10.1029/1999GL008383>
- Horrocks, L. A., Oppenheimer, C., Burton, M. R., Duffell, H. J., Davies, N. M., Martin, N. A., & Bell, W. (2001). Open-path Fourier transform infrared spectroscopy of SO<sub>2</sub>: An empirical error budget analysis, with implications for volcano monitoring. *Journal of Geophysical Research*, 106(D21), 27647–27659. <https://doi.org/10.1029/2001JD000343>
- Horwell, C. J. (2007). Grain-size analysis of volcanic ash for the rapid assessment of respiratory health hazard. *Journal of Environmental Monitoring*, 9(10), 1107–1115. <https://doi.org/10.1039/b710583p>
- Ilyinskaya, E., Martin, R. S., & Oppenheimer, C. (2012). Aerosol formation in basaltic lava fountaining: Eyjafjallajökull volcano, Iceland. *Journal of Geophysical Research*, 117(D20). <https://doi.org/10.1029/2011JD016811>
- Ilyinskaya, E., Schmidt, A., Mather, T. A., Pope, F. D., Witham, C., Baxter, P., et al. (2017). Understanding the environmental impacts of large fissure eruptions: Aerosol and gas emissions from the 2014–2015 Holuhraun eruption (Iceland). *Earth and Planetary Science Letters*, 472, 309–322. <https://doi.org/10.1016/j.epsl.2017.05.025>
- Kroll, J. H., Cross, E. S., Hunter, J. F., Pai, S., Trex, X. I., Trex, X. I., et al. (2015). Atmospheric evolution of sulfur emissions from Kilauea: Real-time measurements of oxidation, dilution, and neutralization within a volcanic plume. *Environmental Science & Technology*, 49(7), 4129–4137. <https://doi.org/10.1021/es506119x>
- Kumar, A., Wu, S., Weise, M. F., Honrath, R., Owen, R. C., Helmig, D., et al. (2013). Free-troposphere ozone and carbon monoxide over the North Atlantic for 2001–2011. *Atmospheric Chemistry and Physics*, 13(24), 12537–12547. <https://doi.org/10.5194/acp-13-12537-2013>
- La Spina, A., Burton, M., Allard, P., Alparone, S., & Muré, F. (2015). Open-path FTIR spectroscopy of magma degassing processes during eight lava fountains on Mount Etna. *Earth and Planetary Science Letters*, 413, 123–134. <https://doi.org/10.1016/j.epsl.2014.12.038>
- La Spina, A., Burton, M., & Salerno, G. G. (2010). Unravelling the processes controlling gas emissions from the central and northeast craters of Mt. Etna. *Journal of Volcanology and Geothermal Research*, 198(3–4), 368–376. <https://doi.org/10.1016/j.jvolgeores.2010.09.018>
- Longo, B. M., Yang, W., Green, J. B., Crosby, F. L., & Crosby, V. L. (2010). Acute health effects associated with exposure to volcanic air pollution (vog) from increased activity at Kilauea Volcano in 2008. *Journal of Toxicology and Environmental Health Part A: Current Issues*, 73(20), 1370–1381. <https://doi.org/10.1080/15287394.2010.497440>
- Lund Myhre, C. E., Christensen, D. H., Nicolaisen, F. M., & Nielsen, C. J. (2003). Spectroscopic study of aqueous H<sub>2</sub>SO<sub>4</sub> at different temperatures and compositions: Variations in dissociation and optical properties. *Journal of Physical Chemistry A*, 107(12), 1979–1991. <https://doi.org/10.1021/jp026576n>
- Mather, T. A., Allen, A. G., Oppenheimer, C., Pyle, D. M., & McGonigle, A. J. S. (2003). Size-Resolved characterisation of soluble ions in the particles in the tropospheric plume of Masaya volcano, Nicaragua: Origins and plume processing. *Journal of Atmospheric Chemistry*, 46(3), 207–237. <https://doi.org/10.1023/a:1026327502060>
- Mather, T. A., McCabe, J. R., Rai, V. K., Thieme, M. H., Pyle, D. M., Heaton, T. H. E., et al. (2006). Oxygen and sulfur isotopic composition of volcanic sulfate aerosol at the point of emission. *Journal of Geophysical Research*, 111(D18), 2005JD006584. <https://doi.org/10.1029/2005JD006584>

- Mather, T. A., Tsanev, V. I., Pyle, D. M., McGonigle, A. J. S. S., Oppenheimer, C., & Allen, A. G. (2004). Characterization and evolution of tropospheric plumes from Lascar and Villarrica volcanoes, Chile. *Journal of Geophysical Research*, 109(D21). <https://doi.org/10.1029/2004JD004934>
- McGee, K. A., & Gerlach, T. M. (1998). Airborne volcanic plume measurements using a FTIR spectrometer, Kilauea Volcano, Hawaii. *Geophysical Research Letters*, 25(5), 615–618. <https://doi.org/10.1029/98GL00356>
- Menard, G., Moune, S., Vlastélic, I., Aguilera, F., Valade, S., Bontemps, M., & González, R. (2014). Gas and aerosol emissions from Lascar volcano (Northern Chile): Insights into the origin of gases and their links with the volcanic activity. *Journal of Volcanology and Geothermal Research*, 287, 51–67. <https://doi.org/10.1016/j.jvolgeores.2014.09.004>
- Moretti, R., Métrich, N., Arienzo, I., Di Renzo, V., Aiuppa, A., & Allard, P. (2018). Degassing vs. eruptive styles at Mt. Etna volcano (Sicily, Italy). Part I: Volatile stocking, gas fluxing, and the shift from low-energy to highly explosive basaltic eruptions. *Chemical Geology*, 482, 1–17. <https://doi.org/10.1016/j.chemgeo.2017.09.017>
- Mori, T., & Notsu, K. (1997). Remote CO, COS, CO<sub>2</sub>, SO<sub>2</sub>, HCl detection and temperature estimation of volcanic gas. *Geophysical Research Letters*, 24(16), 2047–2050. <https://doi.org/10.1029/97GL52058>
- Mori, T., Notsu, K., Tohjima, Y., Wakita, H., Nuccio, P. M., & Italiano, F. (1995). Remote detection of fumarolic gas chemistry at Vulcano, Italy, using an FT-IR spectral radiometer. *Earth and Planetary Science Letters*, 134(1–2), 219–224. [https://doi.org/10.1016/0012-821X\(95\)00119-W](https://doi.org/10.1016/0012-821X(95)00119-W)
- Naughton, J. J., Lewis, V., Thomas, D., & Finlayson, J. B. (1975). Fume compositions found at various stages of activity at Kilauea Volcano, Hawaii. *Journal of Geophysical Research*, 80(21), 2963–2966. <https://doi.org/10.1029/JC080i021p02963>
- Notsu, K., Mori, T., Igarashi, G., Tohjima, Y., & Wakita, H. (1993). Infrared spectral radiometer: A new tool for remote measurement of SO<sub>2</sub> of volcanic gas. *Geochemistry Journal*, 27(4/5), 361–366. <https://doi.org/10.2343/geochemj.27.361>
- Oppenheimer, C., Bani, P., Calkins, J. A., Burton, M. R., & Sawyer, G. M. (2006). Rapid FTIR sensing of volcanic gases released by Strombolian explosions at Yasur volcano, Vanuatu. *Applied Physics B*, 85(2–3), 453–460. <https://doi.org/10.1007/s00340-006-2353-4>
- Oppenheimer, C., Francis, P., Burton, M., Maciejewski, A. J. H., & Boardman, L. (1998). Remote measurement of volcanic gases by Fourier transform infrared spectroscopy. *Applied Physics B: Lasers and Optics*, 67(4), 505–515. <https://doi.org/10.1007/s003400050536>
- Pfeffer, M., Bergsson, B., Barsotti, S., Stefánsdóttir, G., Galle, B., Arellano, S., et al. (2018). Ground-based measurements of the 2014–2015 Holuhraun volcanic cloud (Iceland). *Geosciences*, 8(1), 29. <https://doi.org/10.3390/geosciences8010029>
- Prata, A. J., & Kerkmann, J. (2007). Simultaneous retrieval of volcanic ash and SO<sub>2</sub> using MSG-SEVIRI measurements. *Geophysical Research Letters*, 34(5). <https://doi.org/10.1029/2006GL028691>
- Realmuto, V. J., Abrams, M. J., Buongiorno, M. F., & Pieri, D. C. (1994). The use of Multispectral thermal infrared image data to estimate the sulfur-dioxide flux from volcanoes - A case-study from mount Etna, Sicily, July 29, 1986. *Journal of Geophysical Research*, 99(B1), 481–488. <https://doi.org/10.1029/93jb02062>
- Reichle, H. G., Beck, S. M., Haynes, R. E., Hesketh, W. D., Holland, J. A., Hynes, W. D., et al. (1982). Carbon monoxide measurements in the troposphere. *Science*, 218(4576), 1024–1026. <https://doi.org/10.1126/science.218.4576.1024>
- Roberts, T., Dayma, G., & Oppenheimer, C. (2019). Reaction rates control high-temperature chemistry of volcanic gases in air. *Frontiers of Earth Science*, 7, 154. <https://doi.org/10.3389/feart.2019.00154>
- Roberts, T. J., Vignelles, D., Liuzzo, M., Giudice, G., Aiuppa, A., Coltelli, M., et al. (2018). The primary volcanic aerosol emission from Mt Etna: Size-resolved particles with SO<sub>2</sub> and role in plume reactive halogen chemistry. *Geochimica et Cosmochimica Acta*, 222, 74–93. <https://doi.org/10.1016/j.gca.2017.09.040>
- Rothman, L. S., Gordon, I. E., Barbe, A., Benner, D. C., Bernath, P. F., Birk, M., et al. (2009). The HITRAN 2008 molecular spectroscopic database. *Journal of Quantitative Spectroscopy and Radiative Transfer*, 110(9–10), 533–572. <https://doi.org/10.1016/j.jqsrt.2009.02.013>
- Sæmundsson, K., Sigurgeirsson, M. Á., & Friðleifsson, G. Ó. (2020). Geology and structure of the Reykjanes volcanic system, Iceland. *Journal of Volcanology and Geothermal Research*, 391, 106501. <https://doi.org/10.1016/j.jvolgeores.2018.11.022>
- Schmidt, A., Leadbetter, S., Theys, N., Carboni, E., Witham, C. S., Stevenson, J. A., et al. (2015). Satellite detection, long-range transport, and air quality impacts of volcanic sulfur dioxide from the 2014–2015 flood lava eruption at Bárðarbunga (Iceland). *Journal of Geophysical Research: Atmospheres*, 120(18), 9739–9757. <https://doi.org/10.1002/2015JD023638>
- Scott, S., Pfeffer, M., Oppenheimer, C., Bali, E., Lamb, O. D., Barnie, T., et al. (2023). Near-surface magma flow instability drives cyclic lava fountaining at Fagradalsfjall, Iceland. *Nature Communications*, 14(1), 6810. <https://doi.org/10.1038/s41467-023-42569-9>
- Sellitto, P., Guerazzi, H., Carboni, E., Siddans, R., & Burton, M. (2019). Unified observation co-existing volcanic sulphur dioxide and sulphate aerosols using ground-based Fourier transform infrared spectroscopy. *Atmospheric Meas. Tech. Discuss.*, 1–12. <https://doi.org/10.5194/amt-2019-186>
- Sellitto, P., & Legras, B. (2016). Sensitivity of thermal infrared nadir instruments to the chemical and microphysical properties of UTLS secondary sulfate aerosols. *Atmospheric Measurement Techniques*, 9(1), 115–132. <https://doi.org/10.5194/amt-9-115-2016>
- Sigmundsson, F., Parks, M., Hooper, A., Geirsson, H., Vogfjörð, K. S., Drouin, V., et al. (2022). Deformation and seismicity decline before the 2021 Fagradalsfjall eruption. *Nature*, 609(7927), 523–528. <https://doi.org/10.1038/s41586-022-05083-4>
- Sizov, F., Vasiliev, V., Gumenjuk-Sichevska, J., Kamenev, Y. E., Dvoretzky, S., & Mikhailov, N. (2008). MCT detectors: From IR to sub-mm and mm wavelength bands. *SPIE*, 725–733. <https://doi.org/10.1117/12.797436>
- Smekens, J.-F. (2024). jfsmekens/plumeIR: PlumeIR first release. [Software]. <https://doi.org/10.5281/zenodo.10846166>
- Smekens, J.-F., Mather, T., Burton, M., Varnam, M., & Pfeffer, M. (2024). Iceland FTIR data from Smekens et al. *JGR. [Dataset]*. 2024). <https://doi.org/10.5287/ora-dpgrxoxor>
- Smekens, J.-F., Mather, T. A., Burton, M. R., La Spina, A., Kabbabe, K., Esse, B., et al. (2023). Quantification of gas, ash, and sulphate aerosols in volcanic plumes from open path Fourier transform infrared (OP-FTIR) emission measurements at Stromboli volcano, Italy. *Frontiers of Earth Science*, 10, 1005738. <https://doi.org/10.3389/feart.2022.1005738>
- Sumlin, B. J., Heinson, W. R., & Chakrabarty, R. K. (2018). Retrieving the aerosol complex refractive index using PyMieScatt: A Mie computational package with visualization capabilities. *Journal of Quantitative Spectroscopy and Radiative Transfer*, 205, 127–134. <https://doi.org/10.1016/j.jqsrt.2017.10.012>
- Tang, Y., Tong, D. Q., Yang, K., Lee, P., Baker, B., Crawford, A., et al. (2020). Air quality impacts of the 2018 Mt. Kilauea volcano eruption in Hawaii: A regional chemical transport model study with satellite-constrained emissions. *Atmospheric Environment*, 237, 117648. <https://doi.org/10.1016/j.atmosenv.2020.117648>
- Whitty, R. C. W., Ilyinskaya, E., Mason, E., Wieser, P. E., Liu, E. J., Schmidt, A., et al. (2020). Spatial and temporal variations in SO<sub>2</sub> and PM<sub>2.5</sub> levels around Kilauea volcano, Hawai'i during 2007–2018. *Frontiers of Earth Science*, 8, 36. <https://doi.org/10.3389/feart.2020.00036>
- Zelenski, M., Taran, Y., & Galle, B. (2015). High emission rate of sulfuric acid from Bezmyanny volcano, Kamchatka. *Geophysical Research Letters*, 42(17), 7005–7013. <https://doi.org/10.1002/2015GL065340>